Node-Dependent Kinematics Approach for Damage Analysis of Reinforced Concrete Structures

Node-dependent kinematics approach for damage analysis of reinforced concrete structures

Jiahui Shen[1], Mário Rui Arruda[2], Alfonso Pagani *[3], Erasmo Carrera[4], Enrico Zappino[5], Riccardo Augello[6], and Marco Petrolo[7]

[1]PhD student, *Mul*2 Lab, Department of Mechanical and Aerospace Engineering, Politecnico di Torino, Torino, 10129, Italy; email: jiahui.shen@polito.it

[2]Research Associate, CERIS, Instituto Superior Técnico, Universidade de Lisboa, Lisboa, 1049-001, Portugal; email: mario.rui.arruda@edu.ulisboa.pt

[3]Full Professor, *Mul*2 Lab, Department of Mechanical and Aerospace Engineering, Politecnico di Torino, Torino, 10129, Italy; email: alfonso.pagani@polito.it (Corresponding author)

[4]Full Professor, *Mul*2 Lab, Department of Mechanical and Aerospace Engineering, Politecnico di Torino, Torino, 10129, Italy; email: erasmo.carrera@polito.it

[5]Associate Professor, *Mul*2 Lab, Department of Mechanical and Aerospace Engineering, Politecnico di Torino, Torino, 10129, Italy; email: enrico.zappino@polito.it

[6]Assistant Professor, *Mul*2 Lab, Department of Mechanical and Aerospace Engineering, Politecnico di Torino, Torino, 10129, Italy; email: enrico.zappino@polito.it

[7]Associate Professor, *Mul*2 Lab, Department of Mechanical and Aerospace Engineering, Politecnico di Torino, Torino, 10129, Italy; email: enrico.zappino@polito.it

Abstract: Modeling damage behavior in engineering structures is vital, but balancing computational efficiency and accuracy presents a significant challenge. This study introduces an advanced higher-order beam model incorporating a node-dependent kinematics approach, enhancing the efficiency of damage analysis in reinforced concrete structures. The proposed beam model is built in the framework of Carrera Unified Formulation, enabling a three-dimensional displacement field from a one-dimensional beam model via variable cross-sectional

*

expansion functions. The node-dependent kinematics approach allows diverse cross-sectional kinematics at different nodes on the same beam element. Therefore, a customized approach can be applied where critical areas susceptible to localized damage utilize Lagrange polynomials and Component-Wise approach for detailed analysis, while non-critical zones apply lower-order Taylor polynomials to reduce computational resources. The model incorporates a modified Mazars damage model for concrete and Von Mises plasticity for steel. Four numerical assessments show that the proposed beam model with node-dependent kinematics can maintain accuracy while reducing degrees of freedom by $35\% - 60\%$ compared to fully refined models with Lagrange polynomials. Moreover, the node-dependent kinematics only require simple adjustments to the cross-sectional kinematics as necessary without extensive mesh refinement. This scalability significantly simplifies the tuning process of beam models for practical applications.

1 Introduction

Over the past decades, numerous numerical models have been developed for the structural analysis of Reinforced Concrete (RC) structures. Experimental studies (MacGregor et al., 1997) have revealed that RC structures exhibit complex behavior, including concrete cracking and crushing, steel plasticity, and the bond-slip interaction between steel rebars and concrete. Capturing these phenomena in a numerical method demands significant computational resources. Despite the challenges posed by computational requirements, numerical models are still essential in specialized engineering and for conducting parametric studies (Kadhim et al., 2020), which provides a cost-efficient alternative to experimental testing. The crucial aspect of simulating RC structures is choosing appropriate material representations for concrete and steel according to specific application scenarios. Additionally, accurately modeling the interaction between concrete and steel reinforcement remains a significant and ongoing challenge (Ogura et al., 2008).

Currently, two principal approaches (Maekawa et al., 2003) are widely utilized in the simulation of RC structures: the continuum method employing three-dimensional (3D) Finite Element Analysis (FEA) and the frame modeling method. The FEA with continuum method employs 3D solid elements to model concrete, whereas steel rebars are simulated using one-dimensional (1D) beam or truss elements (Earij et al., 2017; Sinaei et al., 2012). Various plasticity theories are applied to capture the behavior of steel rebars (de Souza Neto et al., 2011). Continuum damage models, both isotropic (Mazars, 1984) and anisotropic (Halm and Dragon, 1996), have been proposed and validated for concrete damage behavior. The bond-slip interaction between concrete and steel is addressed by incorporating specialized elements like contact or interface elements (Murcia-Delso and Benson Shing, 2015; Casanova et al., 2012). Although this method achieves reliable accuracy, it demands substantial computational resources, particularly for large-scale structures such as RC bridges (Babazadeh et al., 2015)

Unlike the continuum method, frame elements, including lumped and distributed plasticity methods, are more attractive due to their reduced computational requirements. Among these, the fiber beam element is the most preferred for studying the seismic behavior of RC structures (Taucer et al., 1991; Spacone et al., 1996). In this approach, the section is discretized into multiple fibers, and uniaxial constitutive relations govern each fiber according to materials. Such a method allows for the independent modeling of the nonlinear behavior of concrete and steel. The longitudinal behavior is commonly integrated with the Euler-Bernoulli beam theory, where the shear deformations are neglected (Spacone et al., 1996). Then, the behavior of the entire RC member can be approximated by a limited number of beam elements through standard FE approaches. Notably, it has been reported that a single force-based element can effectively simulate the nonlinear response of a frame member (Neuenhofer and Filippou, 1997). Several approaches have been proposed to include the flexure-shear interaction in the beam-column elements, reviewed in (Ceresa et al., 2007). The first way involves the introduction of shear springs at the end of the element, which is simple and easy for implementation but involves calibrating parameters (D'Ambrisi and Filippou, 1999; Marini and Spacone, 2006). The second method consists of integrating Timoshenko beam theory into the frame element and combined with multi-dimensional material constitutive laws, which ensure the capture of flexure-shear interaction at both material and section levels. Different Timoshenko fiber beam elements have been proposed so far, including displacement-based (Ceresa et al., 2009; Feng et al., 2017), force-based (Petrangeli et al., 1999; Mullapudi and Ayoub, 2013), and mixed formulation-based (Saritas and Filippou, 2009, 2013; Cheng and Shing, 2022). However, classical Timoshenko beam elements often have difficulties accurately capturing nonlinear shear deformation due to the assumption of uniform shear stress or capturing localized phenomena (Urmson and Mander, 2012; Girgin et al., 2018).

The trade-off between accuracy and computational demands is challenging. A potential solution is represented by the higher-order beam theory based on Carrera Unified Formulation (CUF) (Carrera et al., 2014). Within the framework of CUF, 1D beam models are employed to describe the 3D displacement field by using various cross-sectional expansion functions. This CUF-based beam theory provides a robust framework for overcoming limitations encountered in classical beam models without relying on additional assumptions. These Euler-Bernoulli and Timoshenko beam theories are considered particular cases by adjusting kinematics in the CUF framework (Carrera et al., 2011). Compared to the previously mentioned frame elements, a more accurate nonlinear shear effect can be taken into account by this CUF-based beam model. Importantly, it provides 3D results comparable to those of 3D solid elements while maintaining the efficiency of the 1D model, which makes it applicable to complex structures such as these owning discontinuities. This capability is typically beyond the reach of both lumped and distributed plasticity models. Moreover, 3D material constitutive laws are directly employed for structural analysis rather than the requirement for the inelastic element parameters, such as bending moment-curvature relationships in the lumped plasticity model.

The application of CUF-based higher-order beam theories has shown success in static and dynamic analyses across various engineering structures (Carrera et al., 2022; Shen et al., 2022). The Component-Wise (CW) approach, a recent development of CUF, considers the exact geometry and material properties within the calculations. These models incorporating the CW approach, referred to as refined CW models, are particularly beneficial for analyzing composite structures such as RC structures (Carrera et al., 2022; Nagaraj and Maiaru, 2023). In (Shen et al., 2023a), the CW models have demonstrated the capability to predict overall softening behavior in RC beams without stirrups and to capture flexural failure in RC beams with stirrups. However, some small beam elements, whose lengths are equal to the diameter of the stirrups, are periodically employed to represent the stirrups' actual geometry accurately.

This exact representation of stirrups in RC structures demands increased beam element discretization, leading to a significant rise in Degrees of Freedom (DoFs) of refined CW models. Furthermore, when dealing with areas of high-stress gradients, there is an increase in computational expense due to the need for more refined models. In the past, refined models were employed across entire domains (Shen et al., 2023a), which is often unnecessary and leads to computational inefficiencies, mainly when local effects are confined to small regions.

A more effective strategy involves applying the refined models only in the required regions, whereas lower-order or classical models are employed in less critical areas. The challenge of joining two different structural models with incompatible kinematics has been extensively explored, with numerous solutions detailed in (Carrera et al., 2018). In the present study, a new Node-Dependent Kinematics (NDK) approach (Carrera and Zappino, 2017) is introduced in the framework of CUF. This method allows the assignment of distinct kinematic assumptions to different nodes within a single 1D beam element, enhancing accuracy in targeted regions through refined kinematics. A transition element can connect the elements with different kinematics, ensuring displacement continuity via the inherent shape functions in the Finite Element (FE) formulation. The advantage of this approach is that the calculation is still within the CUF framework, and no extra formulations are added, which is beneficial for computational efficiency. Furthermore, the notable scalability of this method can avoid further mesh refinement in FE models for global-local analysis (Carrera et al., 2019; Nagaraj et al., 2023). Although the NDK approach has been previously applied to RC structures (Augello et al., 2023), its use has been limited to linear analysis.

In this context, the current study aims to extend the NDK approach to the damage analysis of RC structures in the framework of the 1D-CUF model. This study employs validated material models, such as the modified Mazars damage model for concrete and Von Mises plasticity for steel. These have demonstrated mesh-independent results in previous researches (Shen et al., 2023b,c). The scope of investigation in this work is not only limited to RC beams but also includes more complex engineering structures. To the authors' knowledge, it is the first time to apply global-local strategies like the NDK approach to the nonlinear damage analysis of RC structures. By employing the NDK approach, regions susceptible to critical damage are modeled with higher refinement. In comparison, the lower class is applied to the rest, thereby saving computational costs while ensuring a relatively high accuracy. Hence, the proposed approach shows considerable potential for real-world engineering applications due to its scalability and the optimal balance between accuracy and computational efficiency.

2 Unified higher-order beam models

In the framework of CUF (Carrera et al., 2014), the 3D displacement field of 1D beam models can be derived using the cross-sectional expansion functions. In this work, the axial direction of a 1D beam model is denoted by y, and x and z represent the coordinates in the cross-sectional plane. Hence, the 3D displacement field of a beam-like structure is expressed as follows:

$$\mathbf{u}(x, y, z) = F_\tau(x, z)\mathbf{u}_\tau(y), \qquad \tau = 1, 2, ..., M \tag{1}$$

where $F_\tau(x, z)$ is the cross-sectional expansion function, $\mathbf{u}_\tau(y)$ denotes the vector of unknown displacements along the beam axis, τ is a summation notation, and M signifies the number of terms in the expansion functions. The selection of a particular expansion characterizes the capabilities of a structural model. Various options for $F_\tau(x, z)$ are thoroughly discussed in (Carrera et al., 2014). For the current analysis, both Taylor and Lagrange polynomial expansions are considered, and their details are provided in the subsequent sections.

2.1 Taylor expansion models

Taylor Expansions (TE) employ the Taylor-like polynomials, with base terms of the form $x^m z^n$, where m and n are positive integers. In general, kinematics based on TE can be named TEn, in which n indicates the order of Taylor-like polynomials. For instance, a second-order TE model (TE2) exploits a parabolic expansion of the Taylor-like polynomials, and the corresponding expansion expansions F_τ are:

$$F_1 = 1, \quad F_2 = x, \quad F_3 = z, \quad F_4 = x^2, \quad F_5 = xz, \quad F_6 = z^2 \tag{2}$$

Then, the 3D displacement field of the second-order TE model can be expressed explicitly:

$$\begin{aligned} u_x(x,y,z) &= u_{x_1} + x u_{x_2} + z u_{x_3} + x^2 u_{x_4} + xz u_{x_5} + z^2 u_{x_6} \\ u_y(x,y,z) &= u_{y_1} + x u_{y_2} + z u_{y_3} + x^2 u_{y_4} + xz u_{y_5} + z^2 u_{y_6} \\ u_z(x,y,z) &= u_{z_1} + x u_{z_2} + z u_{z_3} + x^2 u_{z_4} + xz u_{z_5} + z^2 u_{z_6} \end{aligned} \tag{3}$$

where $u_{x_1}......u_{z_6}$ are unknown displacement variables of the problem.

2.2 Lagrange expansion models

Another class utilizes the Lagrange polynomial as the expansion functions F_τ, named the Lagrange Expansion (LE) model. Within these models, the cross-section can be divided into sub-domains, which are connected with Lagrange Points (LPs). The Lagrange polynomials are usually given in terms of normalized coordinates, and any arbitrary cross-sectional geometry can be described with the help of isoparametric formulation. The simplest quadrilateral Lagrange polynomial is the four-point (L4) set, and the corresponding functions are:

$$F_\tau = \frac{1}{4}(1 + r\, r_\tau)(1 + s\, s_\tau), \quad \tau = 1,2,3,4 \tag{4}$$

where r and s are the normalized coordinates in the natural reference system, and (r_τ, s_τ) are the coordinates of point τ.

Therefore, the 3D displacement of LE model with four-point Lagrange polynomials can be given as:

$$\begin{aligned} u_x(x,y,z) &= F_1 u_{x_1} + F_2 u_{x_2} + F_3 u_{x_3} + F_4 u_{x_4} \\ u_y(x,y,z) &= F_1 u_{y_1} + F_2 u_{y_2} + F_3 u_{y_3} + F_4 u_{y_4} \\ u_z(x,y,z) &= F_1 u_{z_1} + F_2 u_{z_2} + F_3 u_{z_3} + F_4 u_{z_4} \end{aligned} \tag{5}$$

where $u_{x_1}......u_{z_4}$ are unknown variables that are physical translational displacements of each LP.

Eq. (5) results from the interpolation of the displacements derived at LPs. Moreover, in practical applications, one can select from quadratic Lagrange polynomials incorporating nine points (L9) or cubic LEs with sixteen points (L16). The physical translational displacements at the LPs within the cross-section correspond to the model's DoFs. Therefore, higher-order Lagrange polynomials provide enhanced accuracy by offering a more significant number of DoFs through additional LPs.

2.3 Finite element approach

The FEM is employed to solve for axial displacement vectors as described in Eq. (1). Accordingly, the displacement field can be rewritten as:

$$\mathbf{u}(x, y, z) = F_\tau(x, z) N_i(y) \mathbf{u}_{\tau i}, \qquad i = 1, ..., N_{NE} \tag{6}$$

where N_i denotes the shape function associated with beam node i, $u_{\tau i}$ is the nodal displacement vector, and N_{NE} represents the number of nodes within each beam element. Similarly, the virtual variation of the displacement can be expressed as:

$$\delta\mathbf{u}(x, y, z) = \delta\mathbf{u}_{sj} F_s(x, z) N_j(y), \qquad j = 1, ..., N_{NE} \tag{7}$$

The detailed information on beam shape functions can be found in (Carrera et al., 2014). Commonly adopted beam elements include two-node linear (B2), three-node quadratic (B3), and four-node cubic (B4) configurations. Notably, the selection of beam elements is independent of the choice of expansion functions, which is a significant flexibility for 1D CUF models.

The 3D strain field, $\boldsymbol{\varepsilon} = \{\varepsilon_{xx}, \varepsilon_{yy}, \varepsilon_{zz}, \varepsilon_{xy}, \varepsilon_{xz}, \varepsilon_{yz}\}^T$, can be obtained through the strain-displacement relation, which can be expressed in a vectorial notation:

$$\boldsymbol{\varepsilon} = \mathbf{B}\mathbf{u} \tag{8}$$

where $\mathbf{B}$ is the linear differential operator with two contributions:

$$
\mathbf{B} = \mathbf{B}_\Omega + \mathbf{B}_y = \begin{bmatrix} \frac{\partial}{\partial x} & 0 & 0 \\ 0 & 0 & 0 \\ 0 & 0 & \frac{\partial}{\partial z} \\ 0 & \frac{\partial}{\partial x} & 0 \\ \frac{\partial}{\partial z} & 0 & \frac{\partial}{\partial x} \\ 0 & \frac{\partial}{\partial z} & 0 \end{bmatrix} + \begin{bmatrix} 0 & 0 & 0 \\ 0 & \frac{\partial}{\partial y} & 0 \\ 0 & 0 & 0 \\ \frac{\partial}{\partial y} & 0 & 0 \\ 0 & 0 & 0 \\ 0 & 0 & \frac{\partial}{\partial y} \end{bmatrix} \tag{9}
$$

The 3D stress field, $\boldsymbol{\sigma} = \{\sigma_{xx}, \sigma_{yy}, \sigma_{zz}, \sigma_{xy}, \sigma_{xz}, \sigma_{yz}\}^T$, can be calculated through the constitutive relation, which is expressed as:

$$
\boldsymbol{\sigma} = \mathbf{C}_\mathrm{d}\boldsymbol{\varepsilon} \tag{10}
$$

where $\mathbf{C}_\mathrm{d}$ is a 6×6 represents the 6×6 stiffness matrix of the damaged material. This study addresses material nonlinearities resulting from damage, requiring a Newton–Raphson scheme. The secant stiffness matrix is used in the incremental process for its simpler implementation than the tangent stiffness matrix, though this may result in slower convergence. More details on the damage model will be introduced later.

2.4 Component-Wise approach

Due to the previously mentioned physical meaning of Lagrange polynomials, the Component-Wise approach, an extension of 1D-CUF models, has been developed to accurately represent composite structures made of diverse materials (Nagaraj et al., 2022; Kaleel et al., 2018). This approach is also effective for RC structures made of steel and concrete. As depicted in Fig. 1, the cross-section of such structure is discretized into multiple elements according to the material. Here, steel is denoted by the red elements, while concrete is indicated in grey. Lagrange points are assigned at their boundaries to maintain displacement continuity at the interfaces of steel and concrete components. The behavior of RC structures is then modeled with the LEs over the discretized beam elements. This CW approach allows for the independent and simultaneous consideration of actual material and geometric properties of each component, leading to a more accurate representation of the structural behavior.

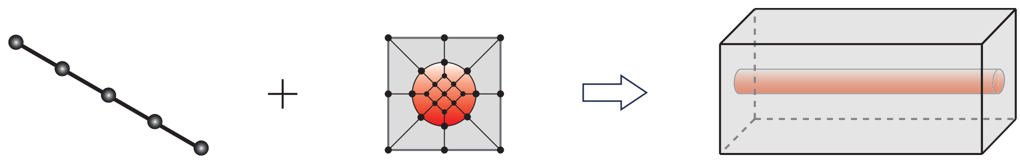

Figure 1: An illustration of the beam model with CW approach for modeling RC structures

3 Node-dependent kinematics approach

According to Section 2, the 3D displacement field of beam elements is first approximated by the cross-sectional expansion $F_\tau(x, z)$ at node i, which is subsequently interpolated along the beam axis using the FE shape functions $N_i(y)$. Typically, uniform cross-sectional expansions are applied across all FE beam nodes. Classical beam theories can be realized in the framework of CUF by designing appropriate cross-sectional expansion. The aforementioned advanced TE and LE can overcome some limitations of these classical theories, particularly in complex scenarios, albeit at an increased computational cost.

In most cases, refined or higher-order models are only required in critical regions of the structure, such as areas with constraints or loadings and zones with concentrated stresses. In contrast, classical or lower-order models are sufficient for the rest of the non-critical regions. This strategy can reduce computational costs under the premise of high accuracy. For the connection between non-critical and critical zones, a node-dependent kinematics approach is proposed for transition. The NDK approach was first introduced in (Carrera and Zappino, 2017) and has since found widespread uses such as (Nagaraj et al., 2023; Scano et al., 2023).

3.1 Beam element with Node-dependent kinematics

An example of a beam structure is illustrated in Fig. 2, where the critical and non-critical regions are denoted by grey and white, respectively. In the NDK framework, the cross-sectional mechanical description $F_\tau(x, z)$ on each node is not uniform anymore, and it is further related to the node i, leading to node-dependent cross-sectional kinematics $F_\tau^i(x, z)$. Consequently, the number of terms in the expansion, M, differs at each node and is replaced with the notation M^i. The displacement fields are smeared through the same FE beam shape functions to ensure displacement continuity across all points. The displacement representation for NDK beam elements, therefore, adopts the following form:

$$\mathbf{u}(x,y,z) = F_\tau^i(x,z)N_i(y)\mathbf{u}_{\tau i}, \qquad i=1,...,N_{NE}; \quad \tau=1,...,M^i \tag{11}$$

Besides, the variation of the corresponding displacement can be written as:

$$\delta\mathbf{u}(x,y,z) = \delta\mathbf{u}_{sj}F_s^j(x,z)N_j(y), \qquad j=1,...,N_{NE}; \quad s=1,...,M^j \tag{12}$$

Figure 2 selects a two-node beam element within the transition zone for demonstration. Assuming the left node, marked in red, adopts a first-order TE while the right node, depicted in black, utilizes a linear LE with four nodes, the displacement field of Eq. (11) can be expressed as:

$$\mathbf{u}(x,y,z) = N_1(y)[\mathbf{u}_{11} + \mathbf{u}_{21}x + \mathbf{u}_{31}z] + N_2(y)[\mathbf{u}_{12}L_1 + \mathbf{u}_{22}L_2 + \mathbf{u}_{32}L_3 + \mathbf{u}_{42}L_4] \tag{13}$$

where L_1......L_4 are Lagrange expression from Eq. (4).

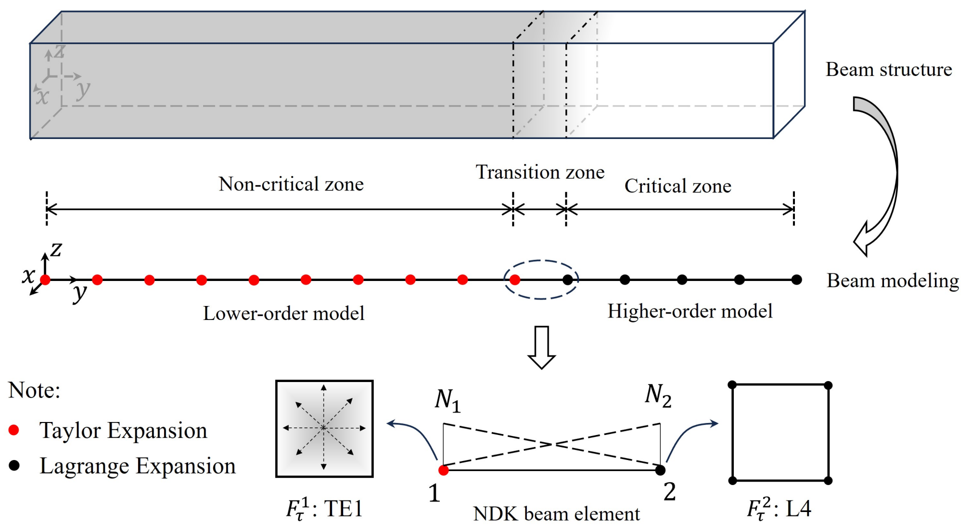

Figure 2: A CUF-based 1D model with NDK approach

3.2 FE governing equations

The governing equation for static problems is derived from the principle of virtual displacements, which states the equality of the external virtual work (δL_{ext}) and internal virtual work

(δL_{int}). For simplicity, they are expressed as:

$$\delta L_{\text{int}} = \int_V \delta \boldsymbol{\varepsilon}^{\mathrm{T}} \boldsymbol{\sigma} \, \mathrm{d}V = \delta \boldsymbol{u}_{sj}^{T} \mathbf{K}^{\tau sij} \mathbf{u}_{\tau i} \tag{14}$$

$$\delta L_{ext} = \int_V \delta \boldsymbol{u}^{\mathrm{T}} \mathbf{F} \, \mathrm{d}V = \delta \boldsymbol{u}_{sj}^{\mathrm{T}} \int_V N_j F_s^j \mathbf{F} \, \mathrm{d}V = \delta \boldsymbol{u}_{sj}^{\mathrm{T}} \mathbf{F}_{sj} \tag{15}$$

with

$$\mathbf{K}^{\tau sij} = \int_l \int_\Omega \left[\mathbf{B}^T (N_j(y) F_s^j(x,z)) \mathbf{C}_{\mathrm{d}} \mathbf{B} (F_\tau^i(x,z) N_i(y)) \right] \mathrm{d}\Omega \mathrm{d}l \tag{16}$$

where $\mathbf{K}^{\tau sij}$ is the fundamental nucleus in the form of 3×3 stiffness matrix; l and Ω represent the length of beam element and area of cross-section respectively; i, j, and τ, s are indexes related to beam shape function and cross-sectional expansion function respectively. $\mathbf{F}$ is the external load and $\mathbf{F}_{sj}$ is the load vector in a 3×1 array. Thus, the governing equation can be expressed as:

$$\mathbf{K}^{\tau sij} \mathbf{u}_{\tau i} = \mathbf{F}_{sj} \tag{17}$$

The matrix $\mathbf{K}^{\tau sij}$ is the basic block from which the stiffness matrix of the whole structure can be constructed automatically. It can be expressed as:

$$\mathbf{K}^{\tau sij} = \begin{bmatrix} k_{xx}^{\tau sij} & k_{xy}^{\tau sij} & k_{xz}^{\tau sij} \\ k_{yx}^{\tau sij} & k_{yy}^{\tau sij} & k_{yz}^{\tau sij} \\ k_{zx}^{\tau sij} & k_{zy}^{\tau sij} & k_{zz}^{\tau sij} \end{bmatrix} \tag{18}$$

Extended forms for each component in Eq. (18) are detailed in (Carrera and Zappino, 2017). For brevity, the explicit expression of the first component $k_{xx}^{\tau sij}$, for an undamaged isotropic material, is given as follows:

$$k_{xx}^{\tau sij} = C_{22} \int_\Omega F_{\tau,x}^i F_{s,x}^j \mathrm{d}\Omega \int_l N_i N_j \mathrm{d}y + C_{66} \int_\Omega F_{\tau,z}^i F_{s,z}^j \mathrm{d}\Omega \int_l N_i N_j \mathrm{d}y + C_{44} \int_\Omega F_\tau^i F_s^j \mathrm{d}\Omega \int_l N_{i,y} N_{j,y} \mathrm{d}y \tag{19}$$

where C_{22}, C_{44}, and C_{66} are components of the material stiffness matrix, typically determined by the material's modulus of elasticity and Poisson's ratio.

4 Modified Mazars damage models

In this section, the isotropic concrete damage model proposed by Mazars (Mazars, 1984) is presented to capture the damage behavior of concrete. The model is modified with the fracture energy regularization technique to alleviate the mesh dependence based on the tensile and compressive constitutive laws (Arruda et al., 2022). The modified Mazars damage model does not consider permanent strains compared to other models. However, it is adequate for the damage analysis of RC structures subjected to quasi-static loads due to the role of steel reinforcement in governing the plastic behavior of such structures. To this end, the Von Mises yield criterion is employed to describe the plasticity of steel reinforcements.

According to (Mazars, 1984), the evolution of isotropic material stiffness is directly controlled by one scalar damage variable d, which ranges from 0 to 1.0. The formulation of the original Mazars damage model is given as follows:

$$\boldsymbol{\sigma} = \mathbf{C}_{\mathrm{d}}\boldsymbol{\varepsilon} = (1-d)\mathbf{C}\boldsymbol{\varepsilon} \tag{20}$$

where $\mathbf{C}$ represents the material stiffness matrix without damage.

In the Mazars damage model, damage initiation and evolution are governed exclusively by positive strains in the principal directions. Therefore, Mazars introduced an equivalent strain, denoted as ε_{eq}, to cover this behavior. This equivalent strain is calculated according to the following expression:

$$\varepsilon_{eq}(\boldsymbol{\varepsilon}) = \sqrt{\sum_{i=1}^{3} \langle \varepsilon_i \rangle_+{}^2} \tag{21}$$

in which $\langle \cdot \rangle_+$ is the Macauley bracket for picking out the positive value, and ε_i are the principle strains.

Subsequently, the loading function, denoted as $f(\boldsymbol{\varepsilon}, \kappa) = \varepsilon_{eq}(\boldsymbol{\varepsilon}) - \kappa$, depends on the equivalent strain and a damage threshold κ. Before damage occurrence, κ is a material constant that equals the ultimate tensile strain. After damage initiation, it is updated to the current value of ε_{eq}. If $f(\boldsymbol{\varepsilon}, \kappa) = 0$ occurs, it indicates the onset of damage, requiring an update to the damage variable. This update is governed by a linear combination of tensile and compressive damage variables d_t and d_c, and the formulation is expressed as:

$$d = \alpha_{\mathrm{t}} d_{\mathrm{t}} + \alpha_{\mathrm{c}} d_{\mathrm{c}} \tag{22}$$

where α_{t} and α_{c} are weights factors for the tensile and compressive damage variables, d_{t} and compression d_{c}, respectively. The explicit calculation of α_{t} and α_{c} can be found in (Arruda et al., 2022).

Rather than using original damage propagation laws for d_{t} and d_{c} from (Mazars, 1984), this work adopts modified damage evolution laws based on concrete stress-strain relations from fib Model Code 2010 (MC2010) (fib special activity group, 2013), which are more practical. Additionally, a fracture energy regularization technique based on the crack band model is employed to regularize the softening behavior and address the mesh dependency issues.

For tensile responses, the bilinear softening constitutive law from MC2010 may lead to numerical convergence issues when the stress diminishes to zero and the damage ascends to one. To circumvent this, a classical constitutive law with an exponential softening curve is employed. The explicit formulation of tensile damage evolution is derived and expressed as:

$$d_{\mathrm{t}} = g_{\mathrm{t}}\left(\kappa_{\mathrm{t}}\right) = 1 - \frac{\varepsilon_{\mathrm{d0}}}{\kappa_{\mathrm{t}}} \exp\left(\frac{\varepsilon_{\mathrm{d0}} - \kappa_{\mathrm{t}}}{\varepsilon_{\mathrm{tu}} - \varepsilon_{\mathrm{d0}}}\right) \tag{23}$$

where $\varepsilon_{\mathrm{d0}}$ is the threshold elastic strain corresponding to the peak stress, also known as the mean uniaxial tensile strength f_{ctm}; $\varepsilon_{\mathrm{tu}}$ signifies the equivalent ultimate strain for bilinear softening and is associated with the volumetric fracture energy g_{ft} and crack bandwidth l_{c}.

Similarly, the damage evolution law for compression is derived from the compressive stress-strain relationship, which can be expressed as follows:

$$d_{\mathrm{c}} = g_{\mathrm{c}}\left(\kappa_{\mathrm{c}}\right) = \begin{cases} 1 - \dfrac{\left(k \times \eta - \eta^2\right) f_{\mathrm{cm}}}{\left(1 + (k-2) \times \eta\right) E_{\mathrm{cm}} \kappa_{\mathrm{c}}} & \text{if } \kappa_{\mathrm{c}} \leqslant \varepsilon_{\mathrm{c1}} \\ 1 - \dfrac{f_{\mathrm{cm}}}{E_{\mathrm{cm}} \kappa_{\mathrm{c}}} & \text{if } \varepsilon_{\mathrm{c1}} < \kappa_{\mathrm{c}} \leqslant \varepsilon_{\mathrm{c2}} \\ 1 + \dfrac{k_1}{E_{\mathrm{cm}}} - \dfrac{k_2}{E_{\mathrm{cm}} \kappa_{\mathrm{c}}} & \text{if } \varepsilon_{\mathrm{c2}} < \kappa_{\mathrm{c}} \leqslant \varepsilon_{\mathrm{cres}} \\ 1 - \dfrac{\sigma_{\mathrm{cres}}}{E_{\mathrm{cm}} \kappa_{\mathrm{c}}} & \text{if } \varepsilon_{\mathrm{cres}} < \kappa_{\mathrm{c}} \end{cases} \tag{24}$$

with

$$\kappa_{\rm c} = \frac{\kappa_{\rm t}}{\nu\sqrt{2}};\quad \eta = \frac{\kappa_{\rm c}}{\varepsilon_{\rm c1}};\quad k = \frac{1.05E_{\rm cm}\varepsilon_{\rm c1}}{f_{\rm cm}};\quad k_1 = \frac{f_{\rm cm}}{(\varepsilon_{\rm cu} - \varepsilon_{\rm c2})};\quad k_2 = f_{\rm cm} + k_1 \times \varepsilon_{\rm c2};$$

where $f_{\rm cm}$ is the mean compressive strength of the concrete; $E_{\rm cm}$ denotes the secant Young's modulus; k, k_1 and k_2 are parameters from (EN, 2005) to describe the softening part of constitutive laws; $\varepsilon_{\rm c1}$ and $\varepsilon_{\rm c2}$ are strain parameters adopted from (EN, 2005); η is a unidimensional strain ratio provided in (fib special activity group, 2013). $\sigma_{\rm cres}$ is residual compressive stress which ensures stress never reaches 0.0 to avoid convergence issues; $\varepsilon_{\rm cres}$ is the corresponding residual compressive strain; $\varepsilon_{\rm cu}$ is the equivalent ultimate compressive strain when neglecting the residual stress, and is associated with the compressive volumetric fracture energy $g_{\rm fc}$ and crack bandwidth $l_{\rm c}$.

One key issue in fracture energy regularization is determining the correct value of $l_{\rm c}$ for obtaining objective numerical results. It is recognized that various factors, including element shape, element order, and element size, can influence the value of $l_{\rm c}$. In this work, the estimation method of $l_{\rm c}$ from (Shen et al., 2023c) has been adopted. More details of this method can be explored in (Shen et al., 2023c).

5 Numerical examples

This section presents four illustrative examples of reinforced concrete structures selected from existing literature to demonstrate the proposed approach's numerical performance. The first three examples, which focus on RC beams, are based on experimental campaigns and employ a displacement-control method for the numerical simulations. The last example is a numerical model of an RC frame structure.

5.1 Notched reinforced concrete beam under tension

The first example is a direct tension test on a notched RC beam, which was conducted experimentally in (Ouyang et al., 1997). Though the CUF-CW solution has been previously applied to this case (Nagaraj and Maiaru, 2023), further investigation is now placed on NDK models using this simple example. The concrete beam is reinforced with three evenly spaced longitudinal bars. Two notches, each 10 mm deep and 12.7 mm wide, are prefabricated in the middle to initiate the first crack. Fig. 3 depicts the overall load layout and geometries. The left end is fixed in all directions, while a displacement-controlled pressure is applied to the right end. The material properties are adopted from (Nagaraj and Maiaru, 2023) and listed in Table 1.

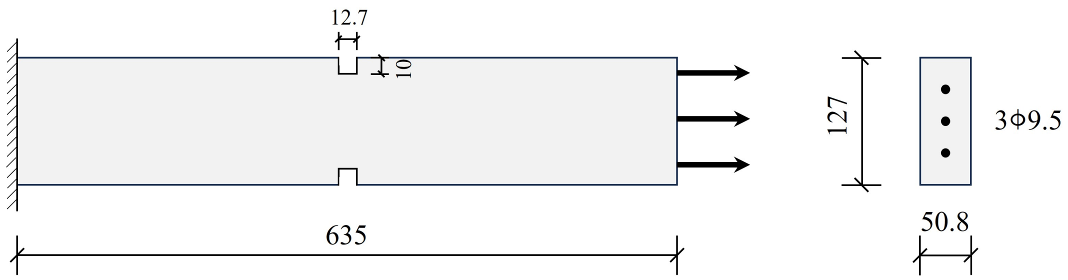

Figure 3: Load layout and geometry of notched RC beams under direct tension (Unit: mm)

Table 1: Material properties of the notched RC beams

Material type	E (GPa)	f_{ctm} (MPa)	f_{cm} (MPa)	G_{ft}(N/m)	G_{fc}(N/m)	υ	f_{y} (MPa)
Concrete	27.349	3.19	44	144	22150	0.175	-
Steel	191.584	-	-	-	-	0.28	508

Beam element discretization is conducted along the longitudinal axis of the structure, with Fig. 4 (a) illustrating that black dots stand for the nodes of beam elements. More beam elements are assigned around the middle notches as suggested from (Nagaraj and Maiaru, 2023). This refinement may be critical for accurately capturing the stress concentration and subsequent damage initiation. Cross-sectional discretizations are visualized in Fig. 4 (b), where red circles represent the steel component within the beam. The steel is integrated into the concrete matrix using LPs so that displacement continuity can be satisfied, which is also the strategy of the CW approach.

In (Nagaraj and Maiaru, 2023), only 5 and 7 quadratic beam elements with quadratic Lagrange elements were employed. Although these models presented satisfactory correlations with experimental load-displacement curves, the limited number of beam elements constrained the prediction of accurate damage distribution. The current analysis employs a finer mesh with 17 quadratic beam elements coupled with the same quadratic Lagrange elements for

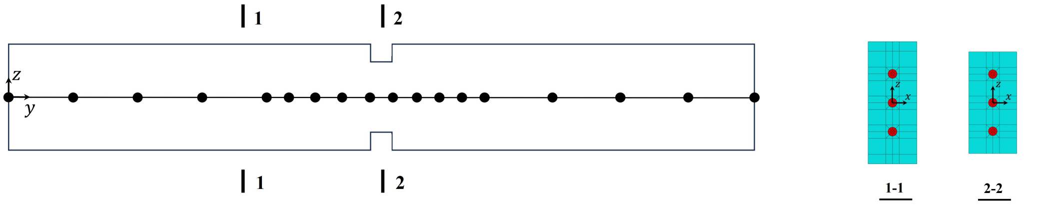

(a) (b)

Figure 4: (a) FE discretization of beam elements and (b) cross-sectional discretization for the notched RC beam

cross-sectional expansion. The beam model in which all nodes are expanded via LEs is named the refined CW model, as depicted in Fig. 5 (a). This model can enhance the numerical accuracy, but the required DoFs are relatively high. For the investigation of the NDK approach, two models are presented in Fig. 5 (b) and (c). Notably, both NDK models adopt an identical mesh discretization to the refined CW model. The difference lies in the expansion functions assigned to specific beam nodes as needed. For instance, TEs are utilized for the beam element nodes with cyan in Fig. 5 (b) and (c), and LEs are employed for the remaining nodes. Compared to the NDK1 model, the NDK2 model tries to increase the number of beam nodes using TEs, further reducing computational expenses. Moreover, the influence of TE order on the structural analysis is also investigated in this part. All information of different models is listed in Table 2.

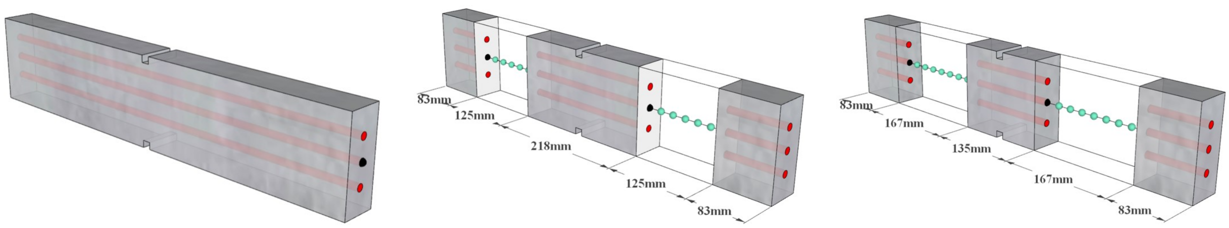

(a) (b) (c)

Figure 5: Different models adopted for the analysis of the notched RC beam: (a) Refined CW model; (b) NDK1 model; (c) NDK2 model

Table 2: Model information of the notched RC beams

Model No.	Model 1	Model 2	Model 3	Model 4	Model 5	Model 6	Model 7
Model type	Refined	NDK1	NDK1	NDK1	NDK2	NDK2	NDK2
TE Order	-	TE1	TE2	TE3	TE1	TE2	TE3
DoFs	43,677	31,257	31,347	31,467	26,289	26,415	26,583

Figure 6 presents the load-deflection responses of the notched RC beam according to the models above, alongside the corresponding experimental results for comparison. The curve of Model 1 agrees well with the experimental data, demonstrating the strong capability of the CW approach in addressing this type of composite structure. Therefore, Model 1 should be regarded as a refined CW model whose performance can be considered a benchmark for NDK models.

When the NDK approach is applied, as illustrated in Figures 6, all NDK models initially exhibit linear behavior identical to that of Model 1. Upon the onset of damage, all NDK models present a consistent structural response. However, the hardening curves of all NDK models are marginally higher than those observed in the experimental data and simulated by Model 1. This slight discrepancy may be attributed to the reduced DoFs in some beam areas. Comparison between Fig. 6 (a) and (b) reveals that the NDK2 model predicts marginally steeper hardening curves, suggesting that the reduction in DoFs has a slight impact on the structural response during hardening.

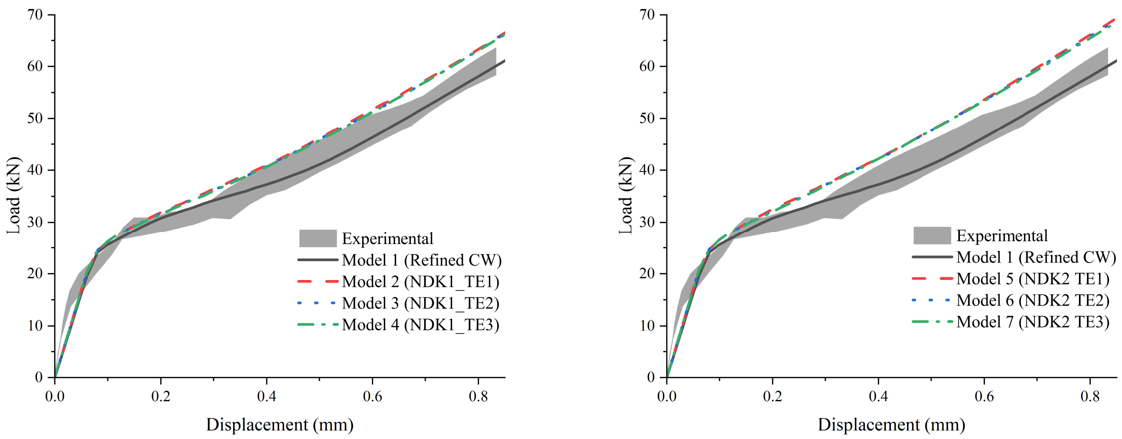

(a) (b)

Figure 6: Load-deflection curves from experimental test, refined CW model, (a) NDK1 models, and (b) NDK2 models for the notched RC beam

To better understand the previously described discrepancy, Fig. 7 presents the final damage distribution for each model. According to Fig. 7 (a), the expected pattern is observed: The entire beam exhibits damage to varying degrees, with a fully damaged zone appearing distinctly and periodically along the beam. The concrete between these zones shows signs of unloading, indicating strain increments are localized in some narrow bands while the rest undergo unloading.

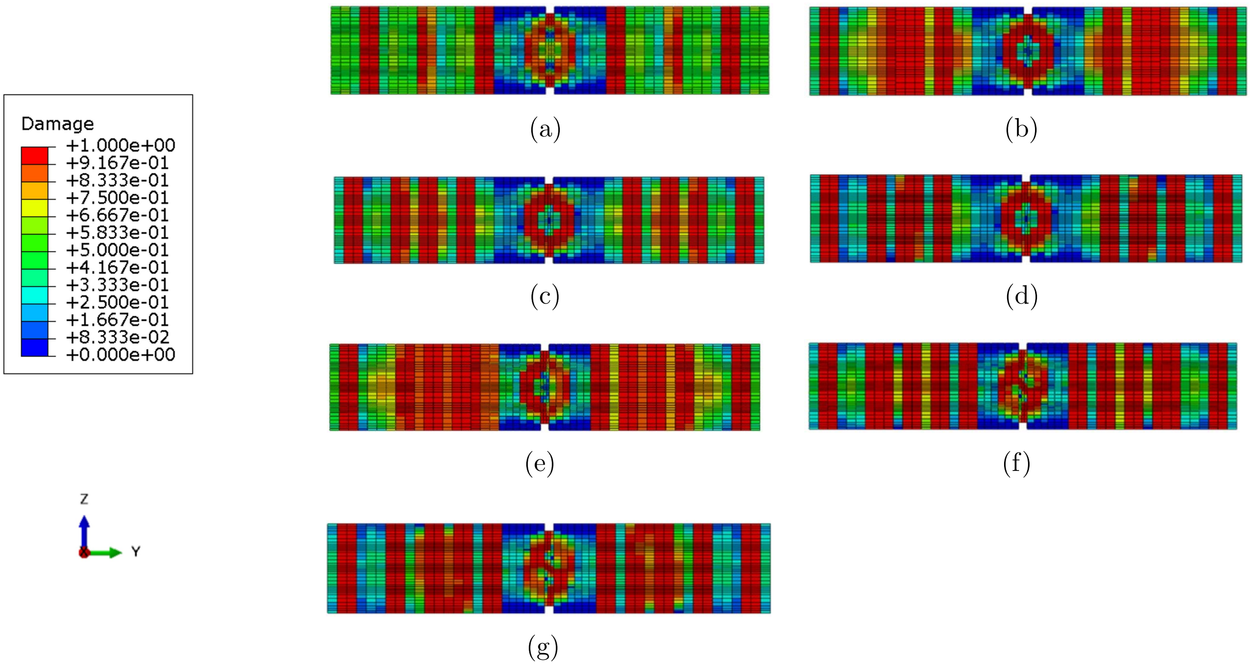

Figure 7: Final damage distributions of the notched RC beam from: (a) Model 1 (Refined CW); (b) Model 2 (NDK1 TE1); (c) Model 3 (NDK1 TE2); (d) Model 4 (NDK1 TE3); (e) Model 5 (NDK2 TE1); (f) Model 6 (NDK2 TE2); (g) Model 7 (NDK2 TE3)

In contrast, Fig. 7 (b) indicates that areas using linear TE are depicted as fully damaged, which may not be reasonable. Applying second-order and third-order TEs to the same areas results in a recurrence of the distributed damage zones, as shown in Figs. 7 (c) and (d), but they are denser than those in Fig. 7 (a). This phenomenon is also observable from Figs. 7 (e) to g.

Therefore, it can be inferred that the NDK models tend to overestimate damage compared to the refined CW model due to the limited DoFs, which further leads to a relatively higher hardening structural behavior. The NDK2 models amplify this phenomenon compared to the NDK1 models due to the increased number of beam elements using TE, which can account for the slightly higher hardening curves observed in Fig. 7 (b) relative to those from NDK1 models in Fig. 7 (a). Nonetheless, the divergence between the results from NDK models and experimental data or refined CW model is considered acceptable given the computational efficiency benefits. Specifically, the NDK2 model demonstrates an approximate 40% reduction in DoFs compared to the refined CW model, rendering them preferable to the NDK1 model, which offers about 28.4% reduction in DoFs.

5.2 Four-point bending reinforced concrete beam

RC beams under a four-point bending test are commonly seen in experimental campaigns because they reflect typical working conditions of RC beams. A benchmark experiment, as reported in (Firmo et al., 2018), was simulated using a CUF-based higher-order beam model detailed in (Shen et al., 2023a). Although this model in (Shen et al., 2023a) produced mesh-independent results, it still required a relatively large number of DoFs. Therefore, this study reviews the same benchmark. Fig. 8 shows the load layout and geometric details. The concrete beam is reinforced with stirrups every 60 mm throughout the length. A displacement control method with a maximum value of 25 mm is employed for numerical simulations. The material properties are listed in Table. 3.

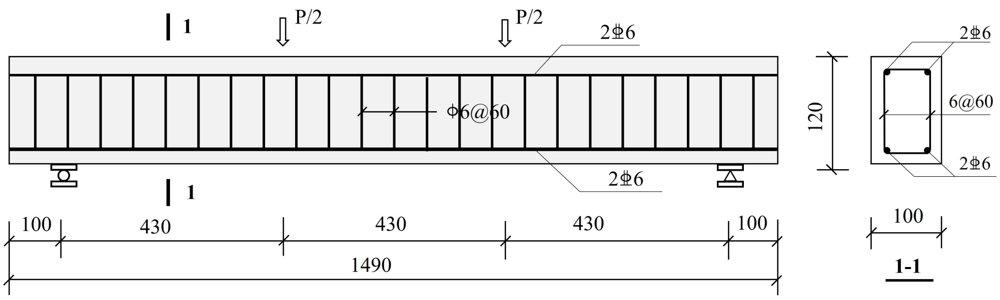

Figure 8: Load layout and geometry of RC beams under four-point bending (Unit: mm)

Table 3: Material properties of the four-point bending RC beam

Material	E (GPa)	f_{ctm} (MPa)	f_{cm} (MPa)	G_{ft}(N/m)	G_{fc}(N/m)	υ	f_{y} (MPa)	f_{yu} (MPa)
Concrete	31.0	2.8	37	140.0	21000	0.2	-	-
Steel	193	-	-	-	-	0.3	546	691

A half-structure model, as depicted in Fig. 9, was utilized for numerical simulation owing to the symmetry. The nodes on the mid-span symmetry plane were restrained against displacement along the axial coordinate. Fig. 9 (a) illustrates the discretization of beam elements, with black dots representing nodes of beam elements. It should be noted that the node positions and quantities are only for illustration rather than for actual numerical calculation. Fig. 9 (b) presents four cross-sectional discretizations, with gray areas representing the elastic plates for loading and support and the red regions denoting steel components. Nodes at the steel-concrete interface are shared to ensure displacement continuity between steel and concrete components.

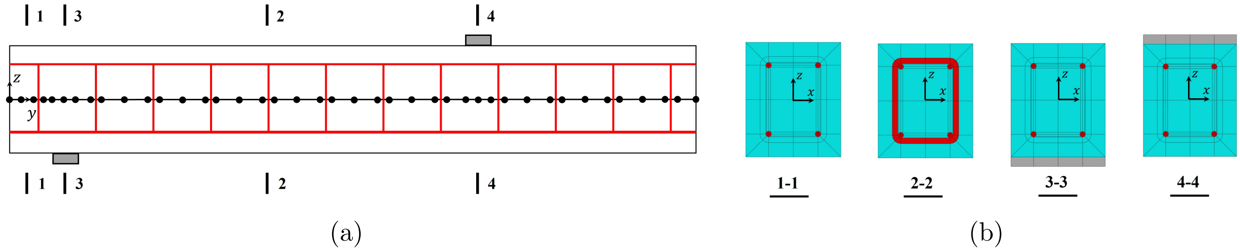

Figure 9: (a) FE discretization of beam elements and (b) cross-sectional discretization for the four-point bending RC beam

To evaluate the efficiency of the NDK solution, Table 4 lists six models where model 1 and model 5 employ LEs for all beam nodes, and the rest adopts the NDK approach. Model 1 and model 5 are acknowledged as refined CW solutions because their accuracies have been confirmed in (Shen et al., 2023a).

Table 4: Model information of the four-point bending RC beam

Model No.	Model 1	Model 2	Model 3	Model 4	Model 5	Model 6
Model type	Refined CW	NDK1	NDK2	NDK3	Refined CW	NDK1
Beam elements	40B2	40B2	40B2	40B2	40B4	40B4
DoFs	55,551	19,263	4,491	4,848	163,743	59,163

Based on the refined CW model, three different NDK models are introduced in Fig. 10, where black nodes are associated with LEs, cyan nodes correspond to TE1, and red nodes indicate TE3. Since the mid-span of bending RC beams is susceptible to damage and failure, NDK1 employs LEs in the mid-span and support zones, while the remaining uses TE1. This strategy ensures detailed damage capture in the critical mid-span region while optimizing computational resources elsewhere. For comparison, NDK2 and NDK3 apply a greedy approach in which only the supporting and loading parts are assigned with LEs and employ TEs elsewhere to highlight the importance of mid-span. It should be noted that all models adhere to the same cross-sectional discretizations as depicted in Fig. 9 (b).

Figure 11 plots the load-deflection response of various models, including the experimental curve for comparison. Initially, there is an excellent agreement between the experimental data and the numerical predictions across all models during the elastic phase. The variance between the numerical and experimental crack loads has been previously discussed in (Shen et al., 2023a). After the elastic step, Models 3 and 4 start to diverge from the expected behavior,

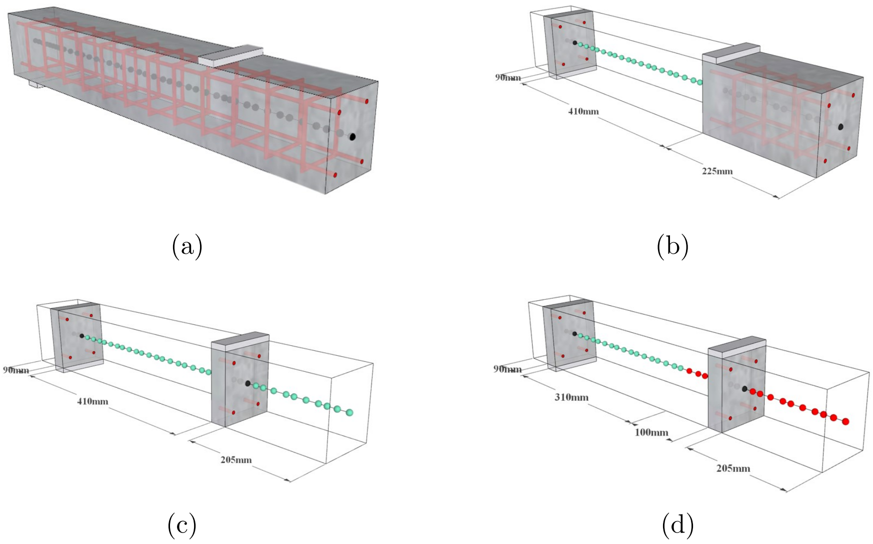

Figure 10: Different models adopted for the analysis of the four-point bending RC beam: (a) Refined CW model; (b) NDK1; (c) NDK2; (d) NDK3. (Cyan stands for TE1 and red represents TE3)

failing to simulate the structural response, particularly after steel yielding accurately. The reason can be found in Figs. 10 (c) and (d), where both models exhibit unreasonable damage compared to Model 1. This inaccuracy results from the inability of TE to provide sufficient DoFs despite the significant reduction in computational demands provided by Models 3 and 4. Consequently, while NDK2 and NDK3 models are applicable for the elastic range, they are too rough to model the correct hardening behavior.

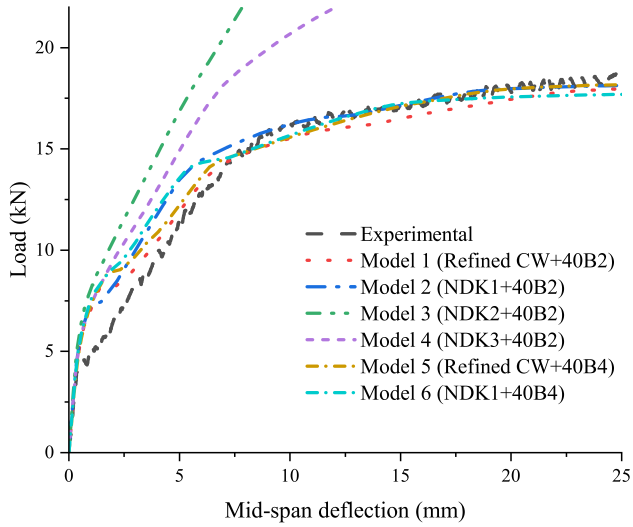

Figure 11: Load-deflection curves for four-point bending RC beams

When comparing the responses from Model 1 and Model 2, as depicted in Fig. 11, the load-deflection curve for the NDK1 model is marginally higher than that of the refined CW model. This variation can be attributed to the reduced DoFs caused by the employment of TE in the shear regions in Model 2, resulting in a stiffer response. As illustrated in Fig. 12, the damage distribution of Model 2 in the shear area is akin to that of Models 3 and 4. However, the damage captured in the mid-span of Model 2 is similar to that of Model 1. Both models capture vertical damage in the tensile zones and compressive damage at the top in the mid-span, which agrees with the experimental crack distribution shown in Fig. 13. Hence, Model 2 can still accurately reflect the load-deflection response, highlighting the greater significance of the structural behavior at the mid-span compared to the shear regions in this structure. A similar observation on load-displacement curves and damage distributions is noted when comparing Models 5 and 6, reinforcing the accuracy of the NDK1 model.

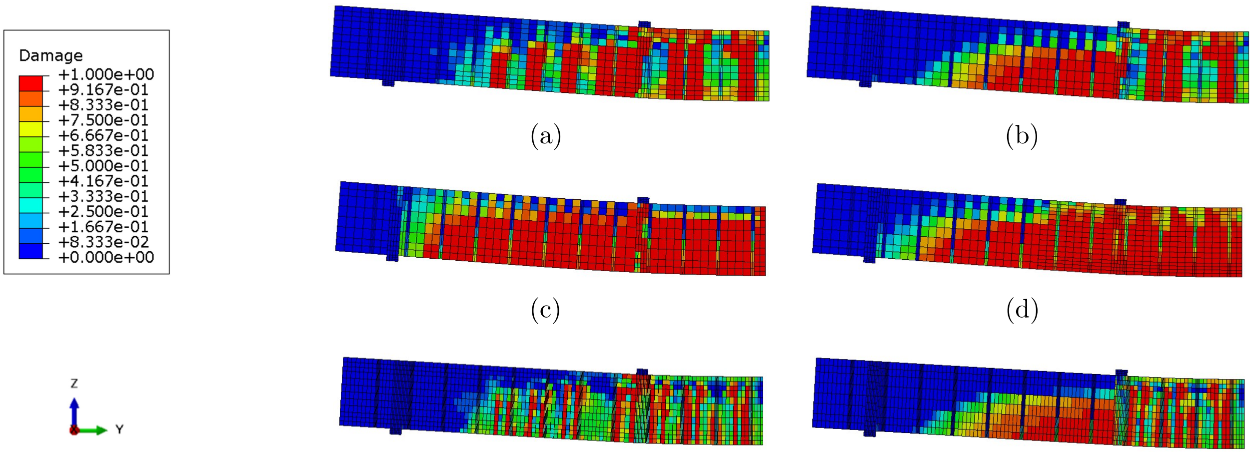

Figure 12: Final damage distribution of four-point bending RC beams from: (a) Model 1 (Refined CW+40B2); (b) Model 2 (NDK1+40B2); (c) Model 3 (NDK2+40B2); (d) Model 4 (NDK3+40B2); (e) Model 5 (Refined CW+40B4); (f) Model 6 (NDK1+40B4)

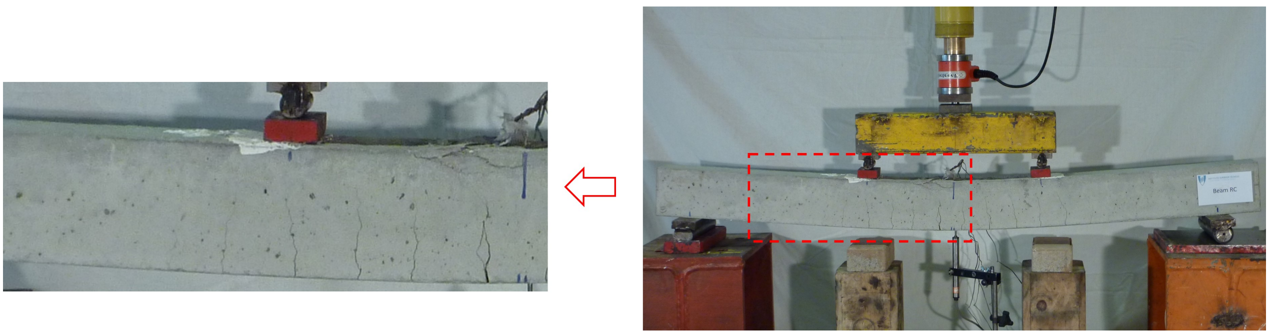

Figure 13: Experimental cracks of four-point bending RC beam (Firmo, 2015)

Additionally, the Von Mises stress distributions of concrete and steel for Models 5 and 6 at the final step are depicted in Fig. 14 and Fig. 15, respectively. The Von Mises stress distributions in the middle span of both models are similar. The Von Mises stresses of concrete in the tensile zones are nearly zero, resulting from tensile strain softening or unloading due to tensile damage. Meanwhile, the Von Mises stresses in the compressive zones reach or approximate the compressive strength, indicating the occurrence of compressive damage. Furthermore, both models demonstrate that the Von Mises stresses in the longitudinal rebars of the bottom layer reach yield stress, as illustrated in Fig. 15. A discrepancy in the stress within the shear zones between the two models can be attributed to the limited DoFs in the shear zones of the NDK models. However, this limitation does not affect the structural performance of the NDK1 model because the investigated RC beam is flexure-dominant, with the mid-span being particularly critical and susceptible to damage. NDK1 model employs higher-order models for the mid-span zone, ensuring its accuracy.

Regarding computational costs, Model 2 exhibits an approximately 65% reduction in DoFs compared to Model 1, while Model 6 offers a similar reduction relative to Model 5. These findings underscore the advantage of the NDK1 model in balancing computational efficiency with high fidelity in structural response simulation.

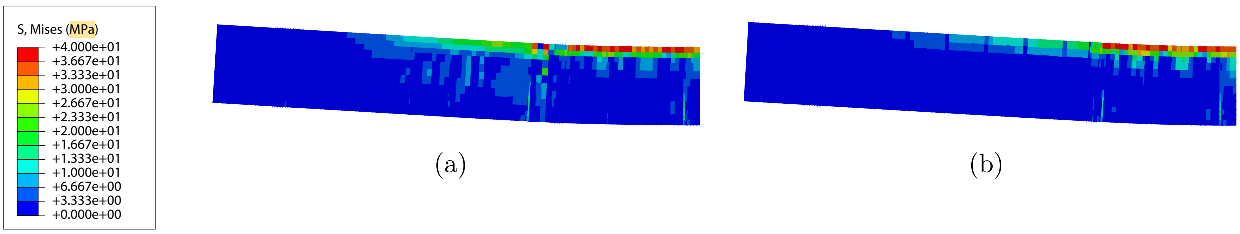

Figure 14: Von Mises stress distribution of concrete in four-point bending RC beam from: (a) Model 5 (Refined CW+40B4); (b) Model 6 (NDK1+40B4) at displacement of 25mm

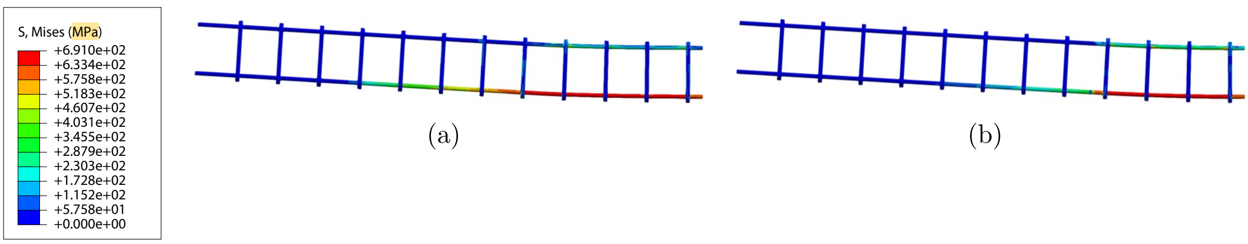

Figure 15: Von Mises stress distribution of steel reinforcement in four-point bending RC beam from: (a) Model 5 (Refined CW+40B4); (b) Model 6 (NDK1+40B4) at displacement of 25mm

5.3 Reinforced concrete beam with web openings

RC beams with web openings are commonly implemented where passing ducts to accommodate vital utilities are necessary. These openings inevitably result in a decrease in stiffness and localized damage, weakening the overall structural performance. A detailed investigation of web openings and their surroundings is important. For this reason, an RC beam with web openings, ideal for applying the NDK approach, is examined as the third case study. A group of experimental campaigns for RC beam with web opening was reported in (Elsanadedy et al., 2019). One selected specimen from (Elsanadedy et al., 2019) is illustrated in Fig. 16, where two rectangular web openings with 450 mm × 225mm are created in the shear zone of the RC beam. The experiment was specifically designed to investigate the response of an RC beam after introducing post-construction openings without any additional strengthening methods. The rest of the experimental conditions are the same as those from the second case. According to (Elsanadedy et al., 2019), the compressive strength of concrete was 50 MPa, measured from cube tests. A strength of 40 MPa is estimated from (fib special activity group, 2013) to align this with cylinder test results. The concrete Young's modulus was unknown; however, preliminary numerical analysis were conducted to approximate the modulus by fitting the experimental linear response. As a result, the concrete's Young's modulus is estimated at 24 GPa. Additional material properties are listed in Table 5.

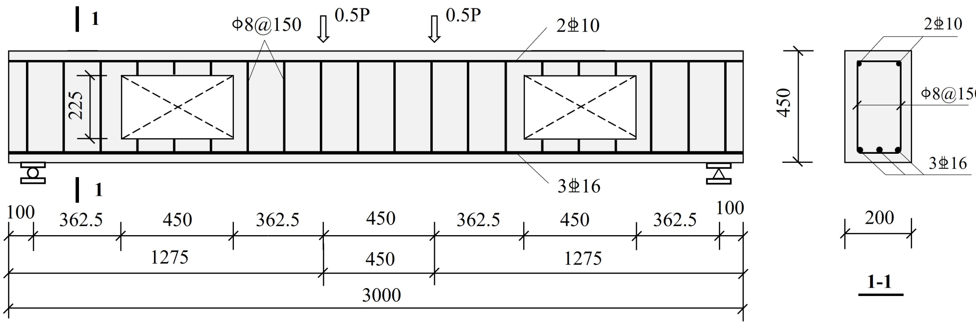

Figure 16: Load layout and geometry of the RC beam with web openings (Unit:mm)

Table 5: Material properties of the RC beam with web openings

Material	E (GPa)	f_{ctm} (MPa)	f_{cm} (MPa)	G_{ft}(N/m)	G_{fc}(N/m)	υ	f_{y} (MPa)
Concrete	24.0	2.3	40	70.0	21627	0.2	-
Steel	200	-	-	-	-	0.3	575

Similarly, only half-structures are modeled for numerical analysis due to the benefit of symmetry. Fig. 17 (a) illustrates the assignment of beam elements, with six distinct cross-sections identified to accommodate stirrups, loading plates, and web openings. Fig. 17 (b) depicts the respective cross-sectional discretizations.

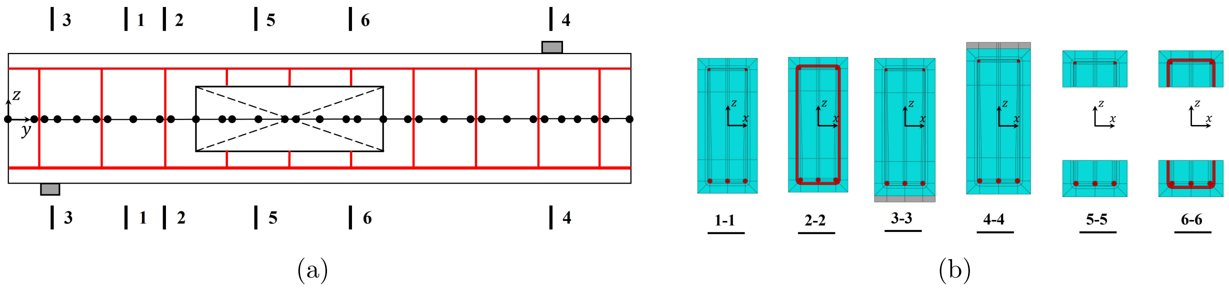

Figure 17: (a) FE discretization of beam elements and (b) cross-sectional discretization for the RC beam with web openings

Four numerical models are designed for the damage analysis, and the corresponding model information is detailed in Table 6. All models employ consistent cross-sectional discretizations and utilize L9 elements when implementing LEs. Model 1 and Model 2 adopt more beam elements than Model 3 and Model 4, ensuring sufficient DoFs for simulations. It is expected that most damage will manifest near the web openings, and some will occur at the bottom of the midspan. Then, one designed NDK model illustrated in Fig. 18 (b) is applied to Models 2 and 4 to demonstrate the effectiveness of the NDK approach. From the previous two examples, the order of TE plays a less important role compared to the length of TE. Therefore, only linear TE is employed where necessary in Models 2 and 4.

Table 6: Model information of the RC beam with web openings

Model No.	Model 1	Model 2	Model 3	Model 4
Model type	Refined CW	NDK	Refined CW	NDK
Beam order	79B2	79B2	42B4	42B4
DoFs	145,641	94,215	231,558	146,820

The load-midspan displacement curves are shown in Fig. 19, comparing numerical simulations and experimental data. Up to a displacement of 3 mm, numerical results closely agree with the experimental data, effectively capturing the linear behavior and initial damage stage. As displacement increases, numerical curves start to deviate from the experimental benchmark. Despite this divergence, the hardening parts of the numerical curves are still

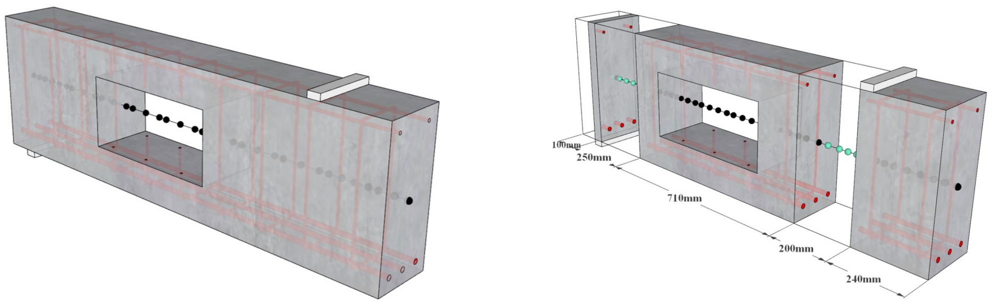

(a) (b)

Figure 18: (a) Refined CW model and (b) NDK model for the analysis of the RC beam with web openings

parallel to the experimental hardening curves. The experimental curve then reaches the peak load and exhibits a sharp drop, whereas the numerical curves do not display a significant decrease. This discrepancy will be explained in the subsequent discussion.

When comparing Model 1 to Model 3, their curves coincide closely until reaching the peak load. The fluctuation in peak loads between these two models is likely due to the difference in employed element approximation, with cubic beam elements providing better precision over linear ones. A similar phenomenon is observed between Model 2 and Model 4. Variations in the results between refined CW models and NDK models are within acceptable ranges because of the utilization of lower-order TE at some beam element nodes, leading to slightly softer numerical models. Nevertheless, the NDK model achieves a significant reduction in the DoFs, approximately 35.3% for B2 elements and 36.6% for B4 elements,

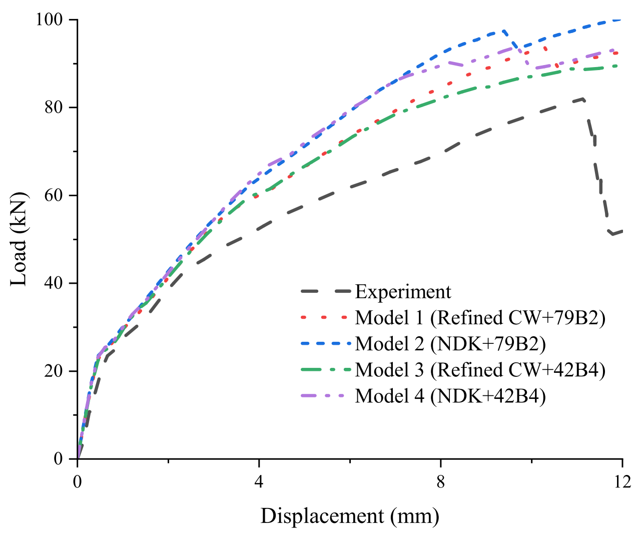

Figure 19: Load-displacement curves for RC beam with web openings

The experimental campaign revealed shear failures in the top and bottom chords, as depicted in Fig. 20, which can explain the sharp drop in reaction load observed in the experimental results shown in Fig. 19. This phenomenon can be attributed to the use of U-shaped stirrups, which reduced bonding effectiveness and caused the concrete in the top and bottom chords to behave similarly to plain concrete, thereby leading to the pronounced diagonal shear cracks observed during the experiment.

However, the numerical damage patterns shown in Fig. 21 fail to replicate these distinct diagonal cracks, which further explains why the numerical models do not exhibit a similar drop in reaction load as observed in the experimental results in Fig. 19. There are two primary reasons for this discrepancy. Firstly, the assumption of a perfect bond between rebars and surrounding concrete in the proposed numerical models allows the stirrups in the chords to continue resisting shear forces, resulting in vertical damage distributions in the opening zones. Secondly, the damage model used in this work only considers Mode 1 failure, making it difficult to capture Mode 2 shear failure accurately.

Although the experimental study detailed in (Elsanadedy et al., 2019) did not report midspan cracks, the numerical models show some damage at the midspan. This discrepancy may be attributed to the damage criterion of the Mazars damage model, which is governed by positive tensile strain and is, therefore, sensitive to tensile damage at the bottom of the midspan. Moreover, some oblique damage distributions are observed close to the opening zones in Fig. 21, which resemble the oblique cracks observed in the same positions in the experimental beam shown in Fig. 20.

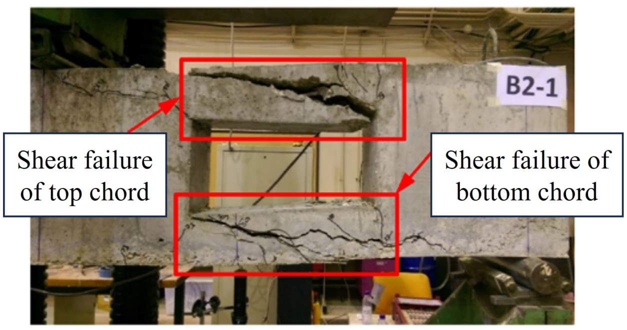

Figure 20: Failures observed from experiments (Elsanadedy et al., 2019)

Implementing the NDK approach results in slight variances in damage distributions for NDK models compared to refined CW models, as shown in Fig. 21. Considering that the web openings are large relative to the whole length of the beam, the damage is evident across most beam regions. Thus, the potential for model improvement is limited, and the employed NDK model likely represents the optimal approach for capturing the damage distribution of this beam.

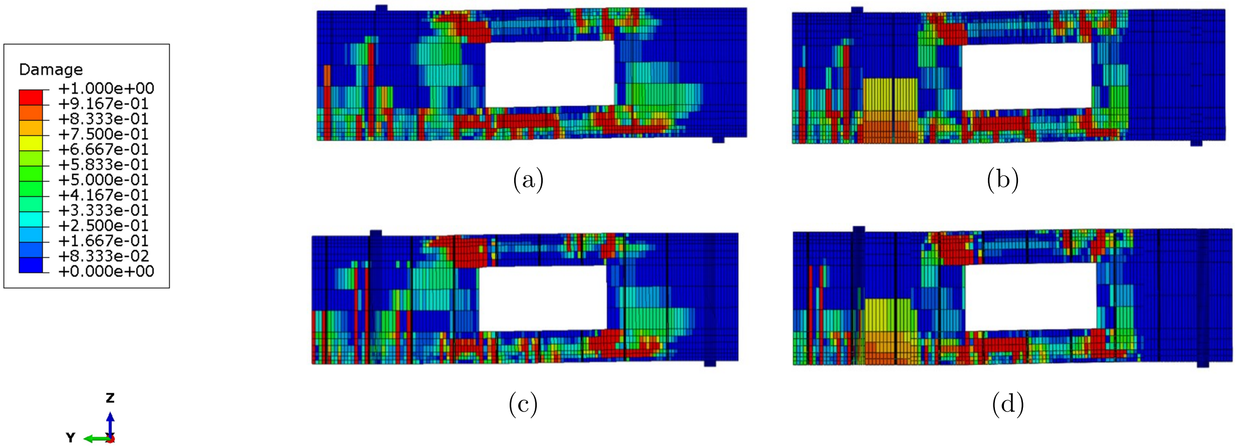

Figure 21: Damage distributions of the RC beam with web openings from: (a) Model 1 (Refined CW+79B2); (b) Model 2 (NDK+79B2); (c) Model 3 (Refined CW+42B4); (d) Model 4 (NDK+42B4) at the displacement of 11 mm

5.4 Reinforced concrete frame

The last example involves a full-scale RC frame to assess the capability of the proposed approach in practical engineering scenarios. The experimental campaign, reported in (Baghi et al., 2018), consisted of three loading phases designed to explore the influence of infill wall on the behavior of RC frame subjected to a column failure. The initial phase involved elastic loading of the RC frame without infill walls, followed by a second phase where the frame infilled with brick walls was loaded until the failure of brick walls. This study specifically considers the third phase, where the infilled wall was removed, and the bare frame was loaded until failure. The RC frame was designed to have strong columns and weak beams according to (EN, 2005). Since the frame was overdesigned and no plastic strains were observed in the longitudinal reinforcement during the first two loading phases, it was assumed to be as new before the third loading phase. The height and width of this frame are around 2.55 m and 5 m, respectively. Fig. 22 depicts the geometry and reinforcement details. A displacement-control method with a maximum value of 150 mm is employed. The material properties are listed in Table. 7.

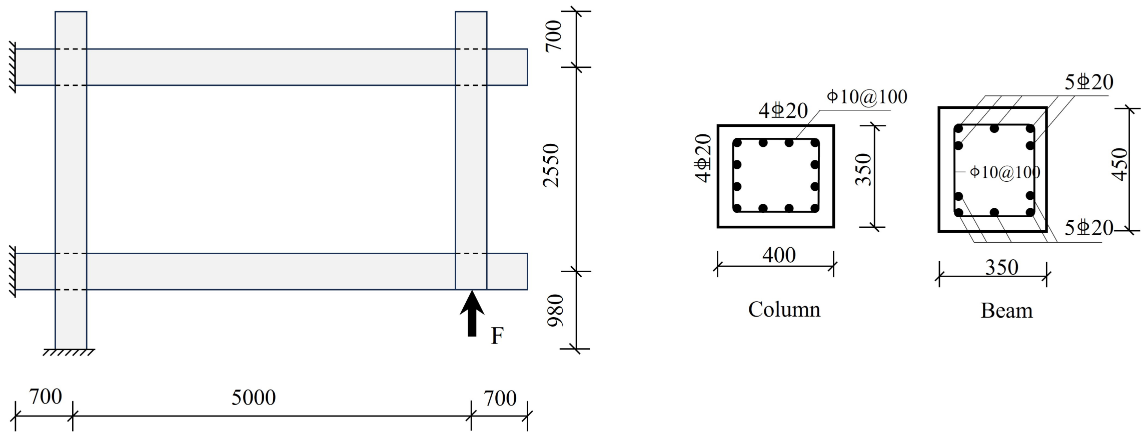

Figure 22: Load layout and geometry of the studied RC frame (Unit: mm)

Table 7: Material properties of the RC frame

Material	E (GPa)	f_{ctm} (MPa)	f_{cm} (MPa)	G_{ft}(N/m)	G_{fc}(N/m)	υ	f_{y} (MPa)	f_{yu} (MPa)
Concrete	36.858	2.7	43	144.0	22000	0.2	-	-
Steel	200	-	-	-	-	0.3	618	720

The structural discretization is detailed in Fig. 23, where beam elements extend along the beam and columns. The black nodes indicating beam element nodes in Fig. 23 (a) are only for illustrative purposes and do not represent their precise locations for calculation. The steel reinforcement within the concrete has been simplified into a square profile while maintaining the same cross-sectional area as its original circular form. This modification not only simplifies the process of cross-sectional discretization but also reduces computational demands. Four distinct cross-sectional discretizations are depicted in Fig. 23 (b) to account for the inclusion of stirrups and the longitudinal rebars from the beam extending into the column. In Fig. 23 (b), the steel is highlighted in red, and the surrounding concrete is designated in cyan. The discretization on the beam cross-section is designed based on the assignment of beam elements along the column, enabling node sharing at the beam-column junction. This design can ensure the displacement continuity at the beam-column connection, especially accounting for the horizontal extension of steel rebars from the beam into the column.

In total, 416 beam elements are required for the entire structure since the periodic placement of stirrups. Four models, detailed in Table 8, are investigated with identical discretizations. However, Model 3 and Model 4 employ quadratic beam elements, and Model 1 and Model 2 adopt linear beam elements. Model 2 and Model 4 apply the NDK approach as depicted in Fig. 24 (b). LEs are mainly used for nodes at beam-column connections, and nodes

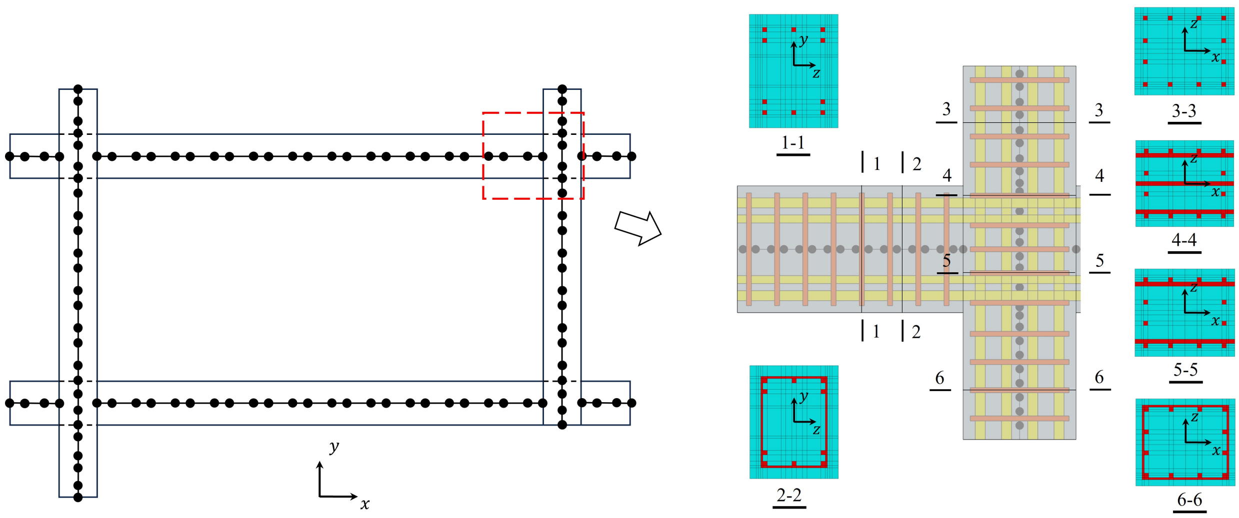

(a) (b)

Figure 23: (a) FE discretization of beam elements and (b) cross-sectional discretization for the RC frame

in the remaining middle sections are defined using linear TE. Moreover, an ABAQUS model is also considered for comparison in which C3D8 solid elements are employed for concrete, and B31 beam elements are adopted for steel. The approximate element size is 40 mm, and 200,598 DOFs are required for this ABAQUS model. Meanwhile, the same modified Mazars damage model is implemented for the ABAQUS model through the UMAT subroutine.

Table 8: Model information of the RC frame

Model No.	Model 1	Model 2	Model 3	Model 4
Model type	Refined CW	NDK	Refined CW	NDK
Beam order	Linear(B2)	Linear(B2)	Quadratic(B3)	Quadratic(B3)
DoFs	328,968	189,684	1,029,240	545,076

The load-deflection diagrams of this RC frame from different numerical models are presented in Fig. 25, in which experimental and numerical results from (Baghi et al., 2018) are included for comparison. All numerical models exhibit apparent deviations in initial stiffness compared to experimental results. However, all numerical models show similar initial stiffness. The discrepancy may be attributed to the formulation of microcracks at the top and bottom beams when the frame was tested in the first phase (Baghi et al., 2018).

Subsequently, the models using modified Mazars damage models in this work, including CUF models and the ABAQUS model, show slight divergences in the crack load compared to

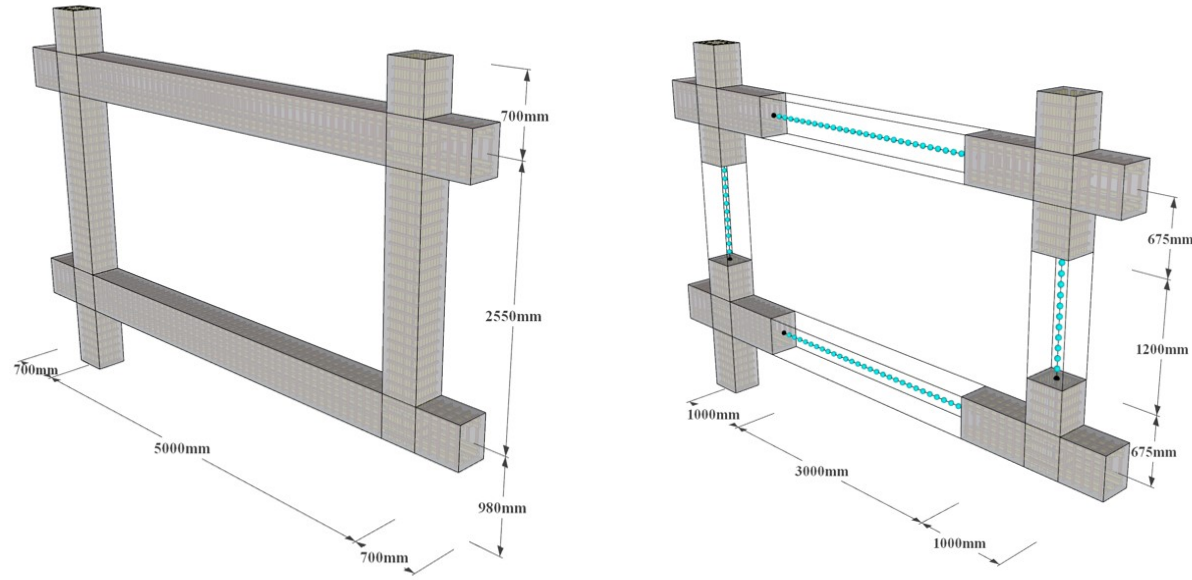

(a) (b)

Figure 24: (a) Refined CW model and (b) NDK model for the analysis of the RC frame

the OpenSees model from (Baghi et al., 2018), which can be attributed to the use of different models. Afterward, all numerical models gradually match the experimental results around the period of steel yielding, when the structural stiffness is further reduced, and the load-displacement curve begins to flatten. In general, the proximity of the CUF models to the ABAQUS and OpenSees models throughout the entire loading process and their alignment with the experimental results in the latter part of the loading process indicates their accuracy.

Minor discrepancies are also observed among different CUF models in Fig. 25. Model 1 and Model 2, which employ the linear beam elements, demonstrate slightly lower curves than Model 3 and Model 4, which adopt the quadratic beam elements. These slight deviations can be attributed to the fact that the characteristic element length might be underestimated for quadratic beam elements, as reported in (Shen et al., 2023c), thus leading to a slightly higher dissipated fracture energy than linear beam elements. Although this sensitivity to element order presents a challenge, the dependency on mesh size can be mitigated through the method from (Shen et al., 2023c). Moreover, Model 2 and Model 4 show marginally higher curves than Model 1 and Model 3, respectively. These observations are consistent with the findings from prior examples due to the lower-order kinematics employed in NDK models.

It was reported that the experimental failure of this bare frame was governed by the formation of plastic hinges from (Baghi et al., 2018), allowing for plastic rotation of beams

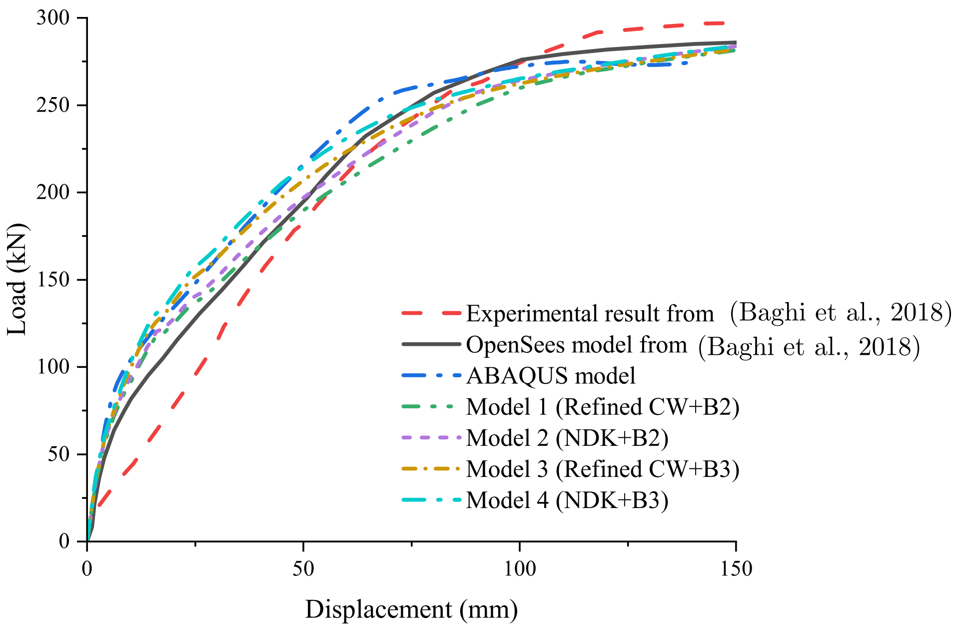

Figure 25: Load-displacement curves for the RC frame

at these critical connection points. Fig 26 depicts the deformation and damage distribution patterns of four CUF models subjected to a displacement of 140 mm, demonstrating similar plastic rotation of beams along their ends.

As experimental cracks were not documented in (Baghi et al., 2018), the corresponding damage distribution of the ABAQUS model, depicted as Fig. 26 (e), is presented as a reference. Damage in beams from Model 1 and Model 2 is continuous and uniform, whereas the ABAQUS model exhibits periodically spaced strip damage. This discrepancy arises from differences in element size between the models. The beam element length in the CUF models for unconfined concrete is approximately 100 mm, while the element size in the ABAQUS model is around 40 mm. Models 3 and 4 with quadratic beam elements display strip damage distributions in the beams similar to those observed in the ABAQUS model. The distinction between Models 1 and 3 is attributed to the different orders of beam elements. In continuum damage models, strain-softening behavior resulting from damage tends to be uniform across the entire linear beam element. In contrast, only part of the quadratic beam element undergoes strain-softening, while the remainder experiences unloading, as reported in (Jirásek and Bauer, 2012).

A minor discrepancy in damage distribution in the middle span of beams between Models 3 and 4 can be observed, attributed to the use of different expansion functions. This phenomenon has similarly been reported in previous comparisons between refined CW and NDK models. Overall, the damage distributions of CUF models align with those from the ABAQUS model, enhancing the accuracy of the proposed method in this work.

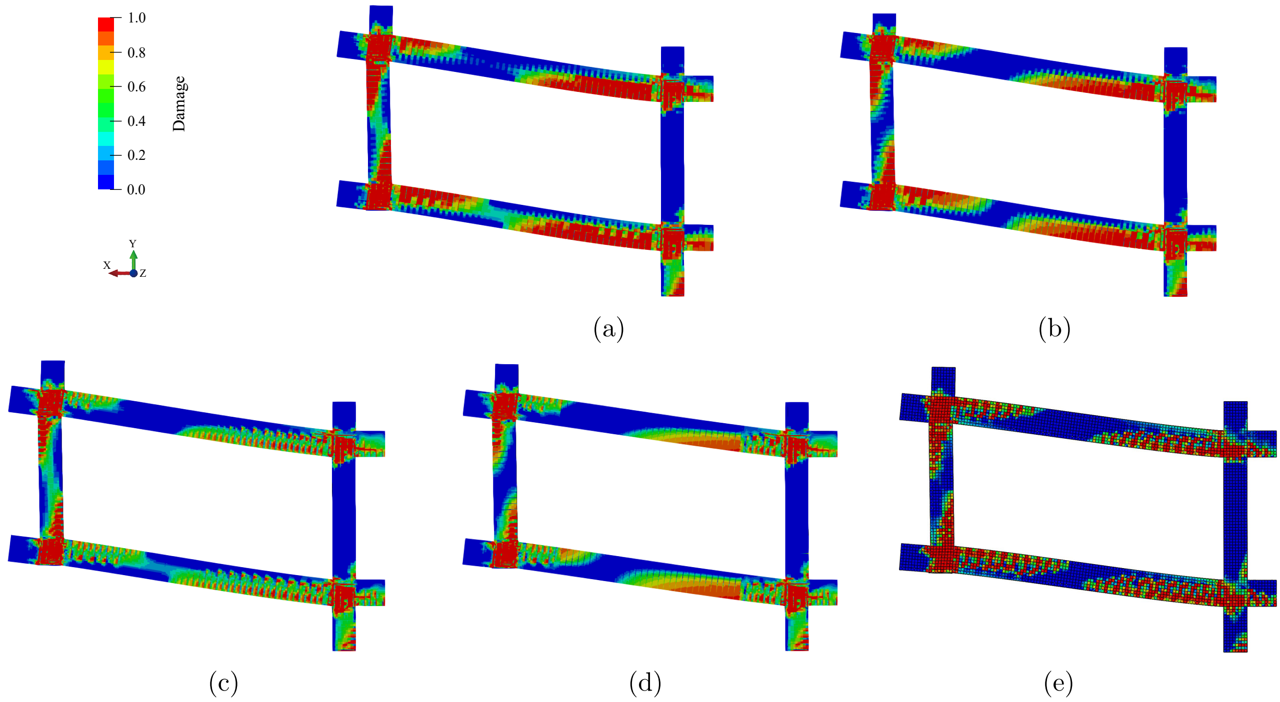

Figure 26: Damage distributions of the frame from: (a) Model 1 (Refined CW+B2); (b) Model 2 (NDK TE1+B2); (c) Model 3 (Refined CW+B3); (d) Model 4 (NDK TE1+B3); (e) ABAQUS model at the displacement of 140 mm (Scale factor is 5)

Regarding computational costs, Model 1 with linear elements requires more DoFs than the ABAQUS model due to the different numerical approaches utilized for reinforcements. Model 1 adopts CUF models that accurately represent the actual geometry of steel components, whereas the ABAQUS model simplifies these components as 1D beam elements. Adopting similar simplifications or lower-order models for steel components may offer further reductions in DoFs, enhancing the efficiency of CUF models in future developments. Nonetheless, incorporating the NDK approach saves significant computational resources, enabling Model 2 to achieve a 42.3% reduction in DoFs compared to Model 1. Additionally, the DoFs needed for Model 2 are about 5% lower than those required by the ABAQUS model. While this 5% reduction may appear modest, the CUF models offer the additional advantage of providing a realistic 3D stress distribution of steel components, enhancing the models' high fidelity. Models 3 and 4 demand a considerable number of DoFs due to the use of higher-order beam elements. However, applying the NDK approach in Model 4 results in approximately a 47% saving in DoFs compared to Model 3. This reduction is significant given the large baseline number of DoFs required by higher-order models.

6 Conclusions

This study presents an NDK approach for 3D global-local damage analysis of reinforced concrete structures, utilizing CUF-based advanced beam models. This approach allows for the application of different kinematic models at each node of the beam element. Specifically, enhanced models can be generated in critical areas using Lagrange polynomials in a CW manner. At the same time, lower-order refinement can be employed for the remaining regions using Taylor polynomials.

For the validation of the proposed NDK models, four complex reinforced concrete structures from existing literature were selected. A modified Mazars damage model for concrete and Von Mises plasticity for steel were applied to these numerical examples. The numerical results have been compared with reference results from the literature, yielding several meaningful conclusions:

1) The NDK approach optimizes beam models by combining the accuracy of local enhancement models with the efficiency of global models, maintaining displacement continuity without special coupling methods.

2) The refined CW model can accurately capture the damage behavior in RC structures, even in complex scenarios such as structures with web openings or full-frame designs. The NDK model demonstrates comparable performance.

3) Regarding computational resources, the NDK models reduce the DoFs by approximately $35\% - 60\%$ compared to the refined CW model for the previous simple cases, signifying a substantial increase in computational efficiency. Notably, when the NDK models are applied to the larger engineering structures, a further significant reduction in computational costs is anticipated.

4) The strong scalability of the NDK models can ensure the realization of diverse NDK models by adjusting the cross-sectional kinematics at the beam element nodes as needed without additional mesh discretization.

Reducing the refined areas in the NDK model can save computational costs at the expense of model accuracy. However, defining these refined areas requires prior knowledge. Excessively large refined regions can lead to insufficient savings in computing resources, whereas refined areas that are too small will result in reduced model accuracy. Therefore, future work will aim to find an automatic model optimization strategy based on the proposed NDK approach. Furthermore, simplifying the representation of stirrups can decrease the total number of required beam elements, enabling constructing a model with computational demands similar to those of widely used fiber models.

Data Availability Statement

Some or all data, models, or code that support the findings of this study are available from the corresponding author upon reasonable request.

Acknowledgement

This work has been partly supported by Foundation for Science and Technology, under the Transitional Standard – DL57/2016/N3/UI/CERIS/CT/165/2018. The author is also grateful for the Foundation for Science and Technology's support through funding UIDB/04625/2020 from the research unit CERIS.

References

Arruda, M., Pacheco, J., Castro, L. M., and Julio, E. (2022). "A modified mazars damage model with energy regularization." *Engineering Fracture Mechanics*, 259, 108129.

Augello, R., Carrera, E., Pagani, A., Arruda, M., and Shen, J. (2023). "Node-dependent kinematic models applied to reinforced concrete structures." *Mathematics and mechanics of complex systems*.

Babazadeh, A., Burgueno, R., and Silva, P. F. (2015). "Use of 3d finite-element models for predicting intermediate damage limit states in rc bridge columns." *Journal of Structural Engineering*, 141(10), 04015012.

Baghi, H., Oliveira, A., Valença, J., Cavaco, E., Neves, L., and Júlio, E. (2018). "Behavior of reinforced concrete frame with masonry infill wall subjected to vertical load." *Engineering Structures*, 171, 476–487.

Carrera, E., Augello, R., Pagani, A., and Xu, X. (2022). "Component-wise approach to reinforced concrete structures." *Mechanics of Advanced Materials and Structures*, 29(25), 3871–3888.

Carrera, E., Fiordilino, G., Nagaraj, M., Pagani, A., and Montemurro, M. (2019). "A global/local approach based on cuf for the accurate and efficient analysis of metallic and composite structures." *Engineering Structures*, 188, 188–201.

Carrera, E., Giunta, G., and Petrolo, M. (2011). *Beam structures: classical and advanced theories*. John Wiley & Sons, Chichester, United Kingdom.

Carrera, E., Petrolo, M., Cinefra, M., and Zappino, E. (2014). *Finite element analysis of structures through unified formulation*. John Wiley & Sons, Chichester, United Kingdom.

Carrera, E. and Zappino, E. (2017). "One-dimensional finite element formulation with node-dependent kinematics." *Computers & Structures*, 192, 114–125.

Carrera, E., Zappino, E., and Li, G. (2018). "Finite element models with node-dependent kinematics for the analysis of composite beam structures." *Composites Part B: Engineering*, 132, 35–48.

Casanova, A., Jason, L., and Davenne, L. (2012). "Bond slip model for the simulation of reinforced concrete structures." *Engineering Structures*, 39, 66–78.

Ceresa, P., Petrini, L., and Pinho, R. (2007). "Flexure-shear fiber beam-column elements for modeling frame structures under seismic loading–state of the art." *Journal of Earthquake Engineering*, 11(S1), 46–88.

Ceresa, P., Petrini, L., Pinho, R., and Sousa, R. (2009). "A fibre flexure–shear model for seismic analysis of rc-framed structures." *Earthquake Engineering & Structural Dynamics*, 38(5), 565–586.

Cheng, J. and Shing, P. B. (2022). "A beam-column element for modeling nonlinear flexural and shear behaviors of reinforced masonry walls." *Earthquake Engineering & Structural Dynamics*, 51(8), 1918–1942.

D'Ambrisi, A. and Filippou, F. C. (1999). "Modeling of cyclic shear behavior in rc members." *Journal of Structural Engineering*, 125(10), 1143–1150.

de Souza Neto, E. A., Peric, D., and Owen, D. R. (2011). *Computational methods for plasticity: theory and applications*. John Wiley & Sons, Chichester, United Kingdom.

Earij, A., Alfano, G., Cashell, K., and Zhou, X. (2017). "Nonlinear three–dimensional finite–element modelling of reinforced–concrete beams: Computational challenges and experimental validation." *Engineering Failure Analysis*, 82, 92–115.

Elsanadedy, H. M., Al-Salloum, Y. A., Almusallam, T. H., Alshenawy, A. O., and Abbas, H. (2019). "Experimental and numerical study on frp-upgraded rc beams with large rectangular web openings in shear zones." *Construction and Building Materials*, 194, 322–343.

(2005). *EN 1992-1-1 Eurocode 2: Design of concrete structures - Part 1-1: General ruels and rules for buildings*, Brussels, Belgium. EN, CEN.

Feng, D.-C., Wu, G., Sun, Z.-Y., and Xu, J.-G. (2017). "A flexure-shear timoshenko fiber beam element based on softened damage-plasticity model." *Engineering Structures*, 140, 483–497.

fib special activity group (2013). *fib model code for concrete structures 2010*. Ernst & Sohn, Wiley, Berlin, Germany.

Firmo, J. (2015). "Fire behaviour of reinforced concrete structures strengthened with cfrp strips." Ph.D. thesis, Instituto Superior Tecnico, Universidade de Lisboa, Lisbon, Portugal.

Firmo, J., Arruda, M., Correia, J., and Rosa, I. (2018). "Three-dimensional finite element modelling of the fire behaviour of insulated rc beams strengthened with ebr and nsm cfrp strips." *Composite Structures*, 183, 124–136.

Girgin, S. C., Moharrami, M., and Koutromanos, I. (2018). "Nonlinear beam-based modeling of rc columns including the effect of reinforcing-bar buckling and rupture." *Earthquake Spectra*, 34(3), 1289–1309.

Halm, D. and Dragon, A. (1996). "A model of anisotropic damage by mesocrack growth; unilateral effect." *International Journal of Damage Mechanics*, 5(4), 384–402.

Jirásek, M. and Bauer, M. (2012). "Numerical aspects of the crack band approach." *Computers & structures*, 110, 60–78.

Kadhim, M. M., Jawdhari, A. R., Altaee, M. J., and Adheem, A. H. (2020). "Finite element modelling and parametric analysis of frp strengthened rc beams under impact load." *Journal of Building Engineering*, 32, 101526.

Kaleel, I., Petrolo, M., and Carrera, E. (2018). "Elastoplastic and progressive failure analysis of fiber-reinforced composites via an efficient nonlinear microscale model." *Aerotecnica Missili & Spazio*, 97, 103–110.

MacGregor, J. G., Wight, J. K., Teng, S., and Irawan, P. (1997). *Reinforced concrete: Mechanics and design*, Vol. 3. Prentice Hall Upper Saddle River, NJ, New Jersey, USA.

Maekawa, K., Okamura, H., and Pimanmas, A. (2003). *Non-linear mechanics of reinforced concrete*. CRC Press, Boca Raton, FL, USA.

Marini, A. and Spacone, E. (2006). "Analysis of reinforced concrete elements including shear effects." *ACI Structural Journal*, 103, 645–655.

Mazars, J. (1984). "Application de la mécanique de l'endommagement au comportement non linéaire et à la rupture du béton de structure." Ph.D. thesis, Université Pierre et Marie Curie Paris 6, Pairs, France.

Mullapudi, T. and Ayoub, A. (2013). "Analysis of reinforced concrete columns subjected to combined axial, flexure, shear, and torsional loads." *Journal of Structural Engineering*, 139(4), 561–573.

Murcia-Delso, J. and Benson Shing, P. (2015). "Bond-slip model for detailed finite-element analysis of reinforced concrete structures." *Journal of Structural Engineering*, 141(4), 04014125.

Nagaraj, M., Carrera, E., and Petrolo, M. (2023). "A global–local approach to the high-fidelity impact analysis of composite structures based on node-dependent kinematics." *Composite Structures*, 304, 116307.

Nagaraj, M., Kaleel, I., Carrera, E., and Petrolo, M. (2022). "Elastoplastic micromechanical analysis of fiber-reinforced composites with defects." *Aerotecnica Missili & Spazio*, 1–7.

Nagaraj, M. and Maiaru, M. (2023). "Progressive damage analysis of steel-reinforced concrete beams using higher-order 1d finite elements." *International Journal for Multiscale Computational Engineering*.

Neuenhofer, A. and Filippou, F. C. (1997). "Evaluation of nonlinear frame finite-element models." *Journal of structural engineering*, 123(7), 958–966.

Ogura, N., Bolander, J. E., and Ichinose, T. (2008). "Analysis of bond splitting failure of deformed bars within structural concrete." *Engineering Structures*, 30(2), 428–435.

Ouyang, C., Wollrab, E., Kulkarni, S., and Shah, S. (1997). "Prediction of cracking response of reinforced concrete tensile members." *Journal of Structural Engineering*, 123(1), 70–78.

Petrangeli, M., Pinto, P. E., and Ciampi, V. (1999). "Fiber element for cyclic bending and shear of rc structures. i: Theory." *Journal of Engineering Mechanics*, 125(9), 994–1001.

Saritas, A. and Filippou, F. C. (2009). "Numerical integration of a class of 3d plastic-damage concrete models and condensation of 3d stress–strain relations for use in beam finite elements." *Engineering Structures*, 31(10), 2327–2336.

Saritas, A. and Filippou, F. C. (2013). "Analysis of rc walls with a mixed formulation frame finite element." *Computers and Concrete*, 12(4), 519–536.

Scano, D., Carrera, E., and Petrolo, M. (2023). "Use of the 3d equilibrium equations in the free-edge analyses for laminated structures with the variable kinematics approach." *Aerotecnica Missili & Spazio*, 1–17.

Shen, J., Arruda, M., Pagani, A., and Carrera, E. (2023a). "A regularized higher-order beam elements for damage analysis of reinforced concrete beams." *Mechanics of Advanced Materials and Structures*, 1–13.

Shen, J., Arruda, M. T., and Pagani, A. (2023b). "Concrete damage analysis based on higher-order beam theories using fracture energy regularization." *Mechanics of Advanced Materials and Structures*, 30(22), 4582–4596.

Shen, J., Pagani, A., Arruda, M., and Carrera, E. (2022). "Exact component-wise solutions for 3d free vibration and stress analysis of hybrid steel–concrete composite beams." *Thin-Walled Structures*, 174, 109094.

Shen, J., Tiago Arruda, M. R., and Pagani, A. (2023c). "A consistent crack bandwidth for higher-order beam theories: Application to concrete." *International Journal of Damage Mechanics*, 10567895231215557.

Sinaei, H., Shariati, M., Abna, A. H., Aghaei, M., and Shariati, A. (2012). "Evaluation of reinforced concrete beam behaviour using finite element analysis by abaqus." *Scientific Research and Essays*, 7(21), 2002–2009.

Spacone, E., Filippou, F. C., and Taucer, F. F. (1996). "Fibre beam–column model for non-linear analysis of r/c frames: Part i. formulation." *Earthquake Engineering & Structural Dynamics*, 25(7), 711–725.

Taucer, F., Spacone, E., and Filippou, F. C. (1991). *A fiber beam-column element for seismic response analysis of reinforced concrete structures*, Vol. 91. Earthquake Engineering Research Center, College of Engineering, University of California Berkekey.

Urmson, C. R. and Mander, J. B. (2012). "Local buckling analysis of longitudinal reinforcing bars." *Journal of Structural Engineering*, 138(1), 62–71.